Grain boundary embrittlement due to phosphorus in tungsten

An atomistic approach

Hiremath, Praveenkumar

Grain boundary embrittlement due to phosphorus in tungsten

An atomistic approach

PRAVEENKUMAR HIREMATH
DEPARTMENT OF MECHANICAL ENGINEERING SCIENCES | LUND UNIVERSITY

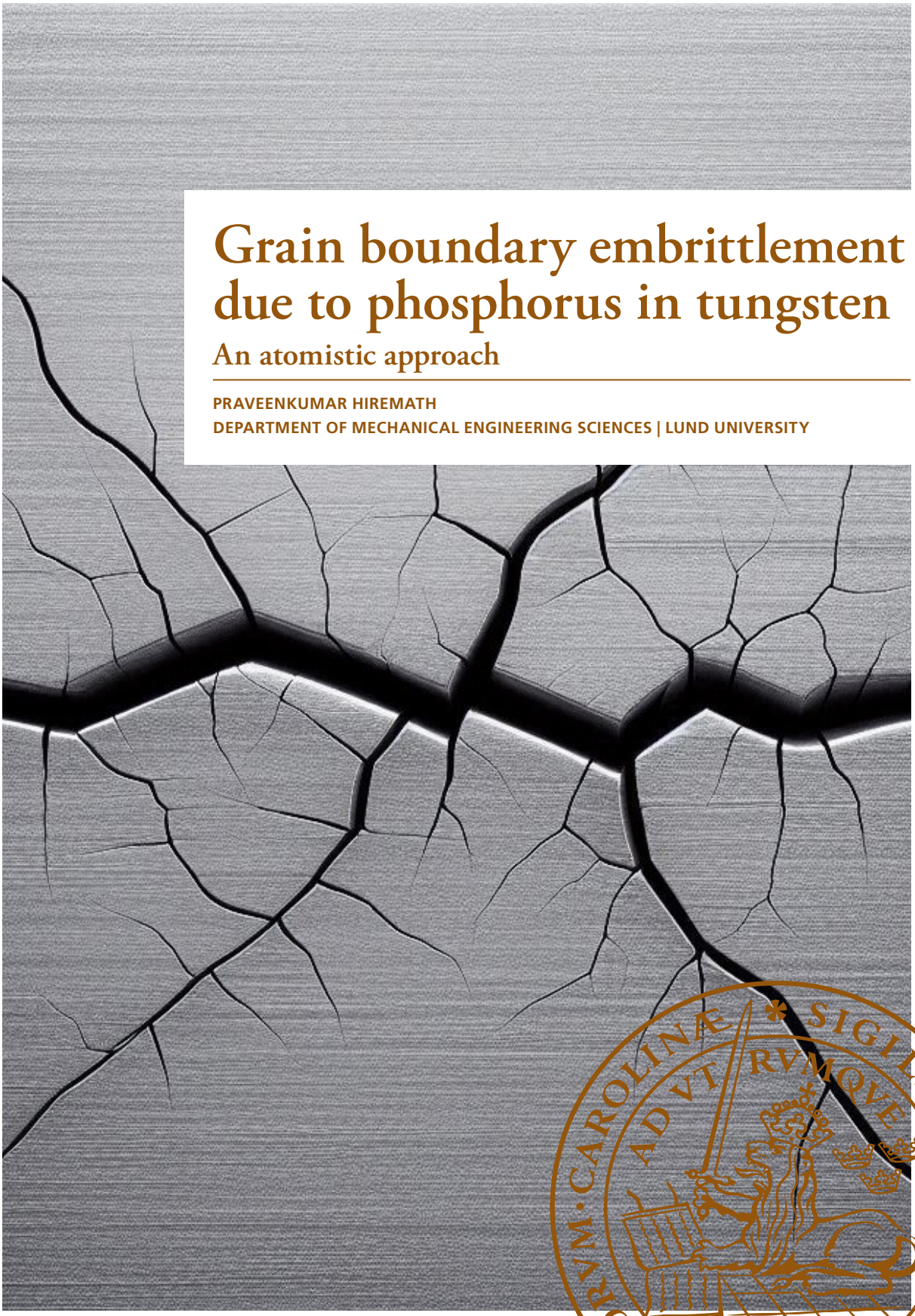

Grain boundary embrittlement due to phosphorus in tungsten

Grain boundary embrittlement due to phosphorus in tungsten

An atomistic approach

by Praveenkumar Hiremath

LUND
UNIVERSITY

Thesis for the degree of Doctorate
Thesis advisors: Dr. Pär A. T. Olsson, Prof. Solveig Melin
Faculty opponent: Doc. Ing. Tomáš Profant

To be presented, with the permission of the Division of Mechanics, Materials & Component Design of Lund University, for public criticism in the M:E lecture hall at the Department of Mechanical Engineering Sciences on Wednesday, the 11th of September 2024 at 9:00.

Organization
LUND UNIVERSITY

Department of Mechanical Engineering Sciences
Box 118
SE–221 00 LUND, Sweden

Document name
DOCTORAL DISSERTATION

Date of disputation
2024-09-11

Sponsoring organization

Author(s)
Praveenkumar Hiremath

Title and subtitle
Grain boundary embrittlement due to phosphorus in tungsten: An atomistic approach

Abstract

Tungsten (W) and its alloys exhibit impressive properties for use in structural components of nuclear fusion reactors. However, impurity induced embrittlement of W grain boundaries (GBs) is a major concern for reactor applications, and necessitates the investigation of the impact of the impurities on the fracture behaviour of the GBs. This work comprises four papers (I-IV) that deal with atomistic modelling of the impact of phosphorus (P) impurities, which is one of the prime embrittlers in W, on the GB cohesion.

The atomistic modelling is performed based on linear elastic fracture mechanics theory. Since interatomic potentials constitute one of the key ingredients for atomistic modelling, a potential that can describe the fracture of W GBs and the embritteling effect of P impurities is recognized in Papers I and II. In Paper II, the impact of P impurities on the GB strength is evaluated. Papers III and IV are concerned with developing atomistic modelling strategies to address the challenges posed by impurities and extract the fracture toughness and scale-independent interfacial excess potential of cracks in GBs.

The results show that the peak stress required for brittle failure of GBs under uniaxial tensile loading is generally reduced in the presence of P impurities. This suggests that the GBs are weakened by the impurities and that the potential in Paper II can capture P induced GB embrittlement. Likewise, the developed modelling strategies successfully evaluate the fracture toughness and scale-independent interfacial excess potential for pristine and P inhabited GB cracks. A decreasing trend is observed in these fracture quantities with increasing P impurity content, which corroborates the embritteling effect of P impurities on GB fracture.

In summary, the present work provides efficient approaches to investigate the influence of P impurities on the fracture behaviour in tungsten GBs, which are general to a degree that they can be applied to other types of impurities too. Additionally, the herein generated interfacial excess potential data can be used for continuum scale studies of higher-timescale fracture phenomena in P inhabited GBs.

Key words
Tungsten, Phosphorus, Impurities, Molecular statics, Molecular dynamics, Monte Carlo, Fracture mechanics, Grain boundaries, Embrittlement.

Classification system and/or index terms (if any)

Supplementary bibliographical information

Language
English

ISSN and key title

ISBN
978-91-8104-078-4 (print)
978-91-8104-079-1 (pdf)

Recipient's notes

Number of pages
170

Price

Security classification

Signature

Date 2024-08-16

Grain boundary embrittlement due to phosphorus in tungsten

An atomistic approach

by Praveenkumar Hiremath

LUND
UNIVERSITY

Cover illustration front: An image illustrating cracks in materials is created by Praveenkumar Hiremath using Image Creator from Microsoft Designer.

Funding information: The thesis work was financially supported by the Swedish Research Council through grants no. 2016-04162, 2018-04348 and 2022-04497.

Division of Mechanics, Materials & Component Design, Department of Mechanical Engineering Sciences

ISBN: 978-91-8104-078-4 (print)
ISBN: 978-91-8104-079-1 (pdf)

Printed in Sweden by Media-Tryck, Lund University, Lund 2024

Dedicated to
my parents and my wife

Contents

List of publications

This thesis is based on the following publications, referred to by their Roman numerals:

I **Effects of interatomic potential on fracture behaviour in single- and bicrystalline tungsten (Published).**
Praveenkumar Hiremath, Solveig Melin, Erik Bitzek, Pär A. T. Olsson
Computational Materials Science 207 (2022) 111283

II **Atomistic investigation of the impact of phosphorus impurities on the tungsten grain boundary decohesion (Published).**
Pär A. T. Olsson, **Praveenkumar Hiremath**, Solveig Melin
Computational Materials Science 219 (2023) 112017

III **Phosphorus driven embrittlement and atomistic crack behaviour in tungsten grain boundaries (Published).**
Praveenkumar Hiremath, Solveig Melin, Pär A. T. Olsson
Computational Materials Science 244 (2024) 113194

IV **Atomistic assessment of interfacial interaction potential in tungsten twist grain boundaries (Submitted for publication).**
Praveenkumar Hiremath, Solveig Melin, Pär A. T. Olsson

Publications not included in this thesis:

V **Ab-initio investigation of mechanical and fracture-related properties of W-Re σ and χ precipitates (Published).**
Anders Vesti, **Praveenkumar Hiremath**, Solveig Melin, Pär A. T. Olsson
Journal of Nuclear Materials 577 (2023) 154261

Acknowledgements

I am thankful to my supervisors: Dr. Pär A. T. Olsson and Prof. Solveig Melin for providing me the opportunity to carry out my Doctoral study at the Department of Mechanical Engineering Sciences, Lund University. I thank them for their support and guidance throughout this project. Especially, Dr. Olsson has helped me develop many skills essential for the research.

I thank Prof. Erik Bitzek at Max-Planck-Institut für Eisenforschung GmbH and FAU Erlangen, Germany, for his contributions to the paper and for sharing his knowledge on atomistic fracture mechanics.

Head of Department, Prof. Aylin Ahadi, thank you for helping me with the administrative matters by giving swift approvals. Many thanks to Mrs. Rose-Marie Hermansson for her assistance with administrative matters, no matter how often I needed it. I am thankful to Dr. Per Hansson and Prof. Jens Wahlström for including me as an assistant in Mechanics courses. It brought me joy and helped me gain useful pedagogical skills. I extend my thanks to Dr. Namsoon Eom for helping me during the Mechanics courses. Additionally, I thank Prof. Jens Wahlström, Dr. Yezhe Lyu and Dr. Rikard Hjelm for always trying to answer my questions regarding the academic profession. I appreciate the initiative Dr. Hjelm took to help PhD students write their theses. I am thankful to Prof. Dmytro Orlov and everyone in the department who attended my presentations. The insightful questions and honest opinions helped me improve my oratory skills. I would also like to thank Prof. Srinivasan Iyengar and Dr. Ralf Denzer for the occasional, yet valuable chats over the years.

I thank my office mates and PhD colleagues for the cordial workspace and for helping me see the academic field from different perspectives. Additionally, I thank the Swedish Research Council for funding the project and NAISS/SNIC for providing the computational resources. I would also like to express my appreciation for the learning resources provided by Lund University and thank everyone involved in the administration of the University.

Oliver, David and Anita, thank you all, for your great hospitality.

And most importantly, I am grateful to my parents for their unconditional support all my life. My wife, all I can tell you is I love you. I am grateful to my parents-in-law for their kind and encouraging words. I am grateful to my sister-in-law for sharing pictures of my nephews (M and P) who have always put a smile on my face. I appreciate my cousin who arranged time for my calls to cheerful nephew (A), despite the time difference.

Popular science summary in English

Tungsten and its alloys are the suggested materials for structural components in nuclear fusion reactors. Despite several attractive properties, tungsten is semi-brittle, characterized by highly brittle behaviour with occasional plastic deformations. Consequently, pre-existing cracks can potentially grow in a brittle manner, ultimately leading to fracture. Some impurities in tungsten weaken it further, by accumulating at locations such as grain boundaries. The impurities therein alter the local mechanical properties, which translates to affect the overall macroscopic response of the material. In particular, phosphorus (P) impurities are known to be one of the prime contributors to the weakening of tungsten through grain boundary embrittlement, which promotes brittle failure. The brittle fracture of structural components can lead to catastrophic nuclear reactor failure, warranting a comprehensive examination of the fracture behaviour of tungsten. The present computational study is aimed at investigating the mechanics behind the fracture behaviour of cracks in tungsten grain boundaries as influenced by P impurities and quantifying the effects.

Studying an individual grain boundary experimentally has proven to be very challenging. That being the case, insights into the fracture behaviour of individual grain boundaries can beneficially be gained by the use of computational methods. They enable comprehension of the physics driving the fracture behaviour, which otherwise may be hidden in experiments. However, predicting how a crack would react to applied loading is a complicated task, even with computational approaches. The available approaches have embraced some assumptions to shed light on grain boundary fracture. The assumptions on many occasions oversimplify the actual grain boundary fracture scenario, making the derived conclusions valid only under specific conditions. Additionally, there is a need to manage the challenges arising due to impurities to better reveal the mechanics of the evolution of pre-existing cracks. Thus, improved computational approaches are sought after.

The approaches presented herein rely on fewer assumptions to mimic the grain boundary crack scenario, all the while the impact of P impurities on the grain boundary crack response is assessed. Based on these developed approaches, it is found that brittle fracture is the dominant mode of failure in pristine grain boundaries. In line with experiments, this study also shows that the phosphorus impurities bring about grain boundary embrittlement and these effects are quantified in terms of the reduction in load required for the cracks to grow. Such data can e.g. be used for model upscaling to study intergranular failure on a microscopic level. Although this work focuses on the embritteling effect of P, the computational approaches are general, and can be used to investigate the role of other impurities in tungsten grain boundary fracture.

1 Introduction

1.1 Background

The ever-growing energy demand and the urgent need to limit the impact on the climate, have triggered a surge towards exploration of newer techniques to harness energy. Nuclear fusion technology has emerged as one of the most promising in this regard [1, 2]. In nuclear fusion reactors, energy released during an initial endothermic fusion of light materials into heavier materials is harnessed. Once the fusion sets in, it is self-sustainable. This attractive technology has paved the way for huge investments in nuclear fusion reactors like the International Thermonuclear Experimental Reactor (ITER) and its successor, the planned Demonstration Power Plant (DEMO) [2].

Choosing appropriate materials for this specific application is very important to bring out its full potential. One of the major challenges in nuclear fusion reactors is to identify materials that are suitable for applications in the plasma facing components (PFC), which are required to withstand the harsh environment of the reactor. The plasma-facing reactor wall in ITER will, in general, be subjected to steady state thermal loads of a few tens of MW/m^2, which during thermal transients, such as plasma disruptions, can be as high as the order of GW/m^2 [3, 4, 5]. Further, irradiation of the plasma-facing surface from high energy neutrons can lead to microstructural damage-induced embrittlement and promote premature propagation of existing cracks in the armour materials [3]. Among the many materials studied to date, tungsten (W) and its alloys have emerged as promising candidates due to their attributes like high melting temperature, high-temperature strength, high thermal conductivity, low thermal expansion coefficient and high sputtering resistance [1, 2, 6, 7, 8, 9, 10, 11, 12]. For example, in DEMO W and W-based alloys can be used as armour materials [8] that form a plasma-facing layer around the first wall. The first wall protects the underlying structural materials, which in the case of DEMO are expected to comprise ferritic-martensitic-9%Cr steels [8]. Tungsten can also be used in cooled plasma-facing mono-block components that make up the diverter of fusion reactors [8], which will be subjected to severe thermal loads [11, 13, 14, 15].

Despite the attractive properties, W suffers from limited ductility at low temperatures, high brittle to ductile transition temperature (BDTT) and low recrystallization temperature, which are drawbacks in structural applications [16, 17]. Tungsten is typically ductile in the range ∼700-1200°C and brittle below 300°C with a relatively high BDTT [18]. According to most experimental results reported in the literature, single crystalline W has a BDTT in the range of ∼100-200°C [19, 20]. For polycrystalline forms, the BDTT lies between ∼150-500°C

[13, 17, 18, 20, 21, 22, 23]. However, on rare occasions the transition has been found to occur at room temperature [24]. This is an indication that the microstructure, i.e. the presence of inclusions, voids, texture, different aspects of grain boundaries (GBs), dislocation density and their mobility, and segregation of impurities at defect sites, have a significant influence on the BDTT, thereby making it difficult to predict an exact range of the BDTT [24, 25, 26]. This is further complicated by the notion that the material does not behave in an exclusively brittle manner below the BDTT. In fact, despite being predominantly brittle, occasional observation of ductile mechanisms, such as twinning and dislocation emission, have been found to accompany the cleavage, which suggests a semi-brittle behaviour [27].

Because the anticipated operating temperature of W-based armour materials in ITER lies in the range ∼500-1400°C [3] and that of the diverter components for water cooled operation is ∼200°C [18, 28, 29], there is a risk of structural failure through brittle fracture. This is further promoted by the additional embrittlement of the material following neutron irradiation from the reactor core [30, 31]. Therefore, for improved forecasting of the fracture and safer reactor operation, a comprehensive assessment of the fracture properties of W is indispensable.

Experimental studies of the fracture behaviour of polycrystalline W have revealed that the most dominant mode of failure is brittle intergranular fracture, which limits the fracture toughness of the material [13, 25, 27]. Furthermore, impurities that segregate at the GBs bring about changes in GB cohesion, thereby impacting the fracture properties. The presence of carbon and boron impurities in W GBs is accompanied by increased GB cohesion [32, 33, 34]. However, segregated sulfur, oxygen and phosphorus (P) impurities weaken the GBs, leading to their embrittlement [29, 32, 35, 36]. Especially, P impurities are considered to be the main embrittler for technically pure polycrystalline W as it was observed that the material's ductility lowered with increasing P concentration [29, 36, 37]. Auger spectroscopy analyses also have confirmed that P impurity segregation at GBs is the main cause for brittle behaviour of W [29]. But a newer experimental investigation [25] has indicated that the W materials analyzed therein are not significantly influenced by the GB segregated impurity up to a concentration of ∼20 wppm. Instead, other factors such as the amount of pre-deformation of the material, size and shape of grains, and dislocation density play an important role in determining the fracture behaviour of W. This is an indication that for P impurities to weaken the GBs, their concentration needs to be above a certain threshold.

With regards to the fracture of individual GBs in W, computational techniques such as density functional theory (DFT) and classical molecular statics/dynamics (MS/MD) have been the trusted approaches. They have been used to investigate the behaviour of special coincident site lattice (CSL) symmetric tilt and twist GBs. Although the classical approach in [38] predicts P impurities to promote GB embrittlement, the results from DFT do not unanimously align. While the DFT studies in [26, 39, 40, 41] predicted that P impurities weaken GBs, reports of contrasting observations have also been made [42], where the cohesion improved upon the introduction of P impurities. It is likely that some of these contradicting results can be partly attributed to limitations in the model description, but the fact that the same GBs were not considered in these studies, could also be an indication that the embritteling effect is GB specific. These contradictory observations and reported inconsistent experimental results of the influence of impurities on the fracture behaviour of polycrystalline W prompts further investigation.

1.2 Objectives of the thesis

This study aims to explore the crack-tip behaviour, and to clarify and quantify the role of P impurities on the integrity of W GBs. Brittle failure is the consequence of the breaking of atomic bonds, whereas local atomic displacements dictate the nucleation of dislocations and deformation twins, which are indicators of plasticity. Therefore, the deformation behaviour is inherently determined by the response of atoms, which necessitates atomistic modelling to gain insight into the matter. Thus, in the present study, classical MS/MD modelling was adopted, for which the numerical tool LAMMPS [43, 44] was used. Although this study focuses on the fracture of the W-P binary system, it is anticipated that the approaches provided here will serve as a framework to study the role of other impurities in W. The objectives of the present work are as follows:

- Evaluate existing interatomic potentials for W based on their suitability for atomistic fracture investigations and delineate intrinsic features that govern the performance.
- Develop and implement modelling strategies to quantify the role of P impurities on the fracture mechanical properties of GBs.
- Develop a strategy for extraction of scale-independent traction-separation excess data for cracks in pristine and P segregated GBs that can be used for upscaling to enable continuum scale fracture studies.

2 Atomic scale fracture

The inevitable presence of defects - like cracks - promotes materials' failure in the form of fracture. As the name indicates, fracture mechanics deals with the failure of materials via fracturing that involves the initiation and propagation of loaded cracks creating new traction-free surfaces. Loading of a crack is generally categorized into mode-I, mode-II and mode-III. Mode-I loading describes the application of an uniaxial loading perpendicular to the crack faces. During mode-II loading, the crack faces are sheared (sliding one over the other) with respect to each other in the crack plane. However, if the shearing is out of the crack plane (anti-planar), it is termed mode-III loading [45]. For the majority of this work (Papers I, III, and IV), the focus has been on the response of semi-infinite cracks in single and bicrystals (GBs) under mode-I loading. For this purpose, the framework of linear elastic fracture mechanics (LEFM) is used. Accordingly, the following sections provide a short description of the underlying theory of LEFM, the theoretical model for perfectly brittle fracture by Griffith [46], the phenomenon of lattice and bond trapping [47, 48], and the often-used criterion for crack-tip plasticity by Rice [49, 50].

2.1 Linear elastic fracture mechanics

Linear elastic fracture mechanics is a sub-field of fracture mechanics to study cracks in materials that undergo elastic deformation [45]. However, owing to the localized high stresses, the region immediate to the crack-tip does not follow linear elastic behaviour [45, 51, 52]. This region is called the fracture process zone (FPZ). According to the small scale yielding condition, the region of FPZ of radius R_{FPZ} should be much smaller than the region of radius R_{K_I} around the crack-tip, where the asymptotic fields from LEFM are dominant (K_I-dominant region). When this condition is satisfied, the crack-tip behaviour is dictated by only the asymptotic fields from LEFM and does not rely on the macroscopic loading conditions outside the K_I-dominant region [45, 51, 52]. This implies that LEFM can be applied to the fracture problem at hand, if the small scale yielding condition is satisfied [52].

According to LEFM, the anisotropic mode-I K_I-controlled stress fields under plane strain conditions, see Figure 1, are governed by the stress intensity factor K_I. The non-zero stress components are given by [53, 54, 55, 56],

$$\sigma_{xx} = \frac{K_I}{\sqrt{2\pi r}} \Re\left\{ \left[\frac{\mu_1 \mu_2}{(\mu_1 - \mu_2)} \right] \left[\frac{\mu_2}{(\cos\theta + \mu_2 \sin\theta)^{1/2}} - \frac{\mu_1}{(\cos\theta + \mu_1 \sin\theta)^{1/2}} \right] \right\}, \quad (1)$$

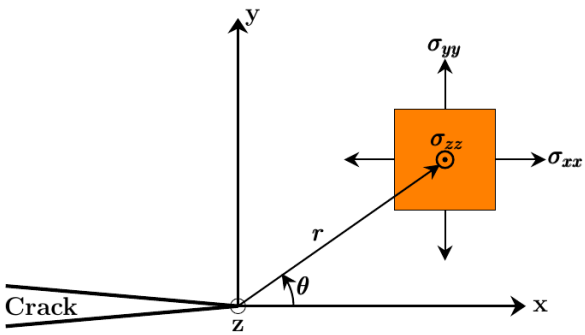

Figure 1: Non-zero stress components at the crack-tip for mode-I loading.

$$\sigma_{yy} = \frac{K_I}{\sqrt{2\pi r}} \Re\left\{ \left[\frac{1}{(\mu_1 - \mu_2)}\right] \left[\frac{\mu_1}{(\cos\theta + \mu_2 \sin\theta)^{1/2}} - \frac{\mu_2}{(\cos\theta + \mu_1 \sin\theta)^{1/2}}\right] \right\}, \quad (2)$$

$$\sigma_{zz} = \frac{K_I}{\sqrt{2\pi r}} \Re\left\{ \left[\frac{\mu_1\mu_2}{(\mu_1 - \mu_2)}\right] \left[\frac{1}{(\cos\theta + \mu_1 \sin\theta)^{1/2}} - \frac{1}{(\cos\theta + \mu_2 \sin\theta)^{1/2}}\right] \right\}, \quad (3)$$

where $\Re$ represents the real part operator. The stress intensity factor depends on the applied load and the crack geometry and is in general given as $K_I = \sigma_0\sqrt{\pi a_{crack}} \cdot f$, where f is a function of crack geometry, σ_0 is the load applied on the boundary, and a_{crack} is the crack length. The complex parameters μ_1 and μ_2 are obtained by solving the characteristic equation

$$s_{11}\mu_j^4 - 2s_{16}\mu_j^3 + (2s_{12} + s_{66})\mu_j^2 - 2s_{26}\mu_j + s_{22} = 0 \quad (4)$$

where s_{ij} are the orientation dependent compliance constants.

The associated displacement fields (u_x and u_y) in the crack-tip vicinity under plane strain conditions can be computed as

$$u_x = \frac{K_I\sqrt{2r}}{\sqrt{\pi}} \Re\left\{ \left[\frac{1}{(\mu_1 - \mu_2)}\right] \left[\mu_1 p_2 (\cos\theta + \mu_2 \sin\theta)^{1/2} - \mu_2 p_1 (\cos\theta + \mu_1 \sin\theta)^{1/2}\right] \right\}, \quad (5)$$

$$u_y = \frac{K_I\sqrt{2r}}{\sqrt{\pi}} \Re\left\{ \left[\frac{1}{(\mu_1 - \mu_2)}\right] \left[\mu_1 q_2 (\cos\theta + \mu_2 \sin\theta)^{1/2} - \mu_2 q_1 (\cos\theta + \mu_1 \sin\theta)^{1/2}\right] \right\}, \quad (6)$$

where,

$$\begin{aligned} p_1 &= s_{11}\mu_1^2 + s_{12} - s_{16}\mu_1, & p_2 &= s_{11}\mu_2^2 + s_{12} - s_{16}\mu_2, \\ q_1 &= \frac{s_{12}\mu_1^2 + s_{22} - s_{26}\mu_1}{\mu_1}, & q_2 &= \frac{s_{12}\mu_2^2 + s_{22} - s_{26}\mu_2}{\mu_2}. \end{aligned} \quad (7)$$

Upon increased loading, a critical stress intensity factor value that initiates crack-tip mechanisms, such as brittle growth or plasticity, will eventually be reached. The critical value corresponding to brittle crack propagation is defined as the fracture toughness and can be forecast as K_{IG} using Griffith's theory for brittle fracture [46]. Similarly, the critical stress intensity factor responsible for the onset of crack-tip plasticity events such as deformation twin formation and dislocation nucleation can be identified as K_{IT} and K_{IE}, respectively, based on Rice's theory [49, 50].

2.2 Crack-tip mechanisms

The occurrence of different crack-tip events is governed by the competition between different mechanisms. According to Griffith's and Rice's theories, any of the mechanisms such as brittle growth, dislocation nucleation or deformation twin formation are feasible for a crack, when the corresponding critical stress intensity factor is the lowest. In this section, an abridged description of both these theories is provided.

2.2.1 Brittle fracture and lattice trapping

Griffith introduced a model to describe brittle failure of materials [46]. According to this model, the theoretical critical stress intensity factor, identified as K_{IG}, of an ideally brittle material subjected to mode-I loading under plane strain conditions is given by [54]

$$K_{IG} = \sqrt{\frac{G_I}{B}}. \tag{8}$$

Here G_I is the energy release rate associated with the formation of two new surfaces and B is the anisotropic compliance constant of the crystal containing a crack in a specific orientation [53, 54]. In the case of an ideally brittle single-crystal, $G_I = 2\gamma_{(klm)}$, with $2\gamma_{(klm)}$ being the total surface energy of the two newly created surfaces with Miller indices (klm), which is equivalent to the ideal work of separation. Along the same lines, G_I^{GB} represents the energy release rate for fracture of an ideally brittle grain boundary and can be expressed as [57, 58]

$$G_I^{GB} = \gamma^1_{(klm)} + \gamma^2_{(k'l'm')} - \gamma_{GB}, \tag{9}$$

where $\gamma^1_{(klm)}$ and $\gamma^2_{(k'l'm')}$ are surface energies of the cleavage surfaces, (klm) and $(k'l'm')$ in grains 1 and 2, respectively, and γ_{GB} is the energy of the GB ground state configuration.

For anisotropic cubic crystals, B can be evaluated as

$$B = \sqrt{\frac{b_{11}b_{22}}{2}\left(\sqrt{\frac{b_{22}}{b_{11}}} + \frac{2b_{12}+b_{66}}{2b_{11}}\right)}, \tag{10}$$

where b_{ij} are the plane strain moduli that are functions of the orientation dependent elastic compliance constants s_{ij}. The b_{ij}s can be computed as [53, 54, 59]

$$\begin{aligned} b_{11} &= \frac{s_{11}s_{33}-s_{13}^2}{s_{33}}, \qquad & b_{22} &= \frac{s_{22}s_{33}-s_{23}^2}{s_{33}}, \\ b_{12} &= \frac{s_{12}s_{33}-s_{13}s_{23}}{s_{33}}, \qquad & b_{66} &= \frac{s_{66}s_{33}-s_{26}^2}{s_{33}}. \end{aligned} \tag{11}$$

Though W is nearly isotropic, the above equations (8)-(11) can still be applied to estimate K_{IG} for it.

Even though Griffith's theory is useful for the prediction of brittle failure, it does not explain crack-front anisotropy. Riedle et al. [60] investigated cracks on preferred cleavage planes, {100} and {110}, in pristine W. They found in their experiments that the cracks have preferential fronts (along z-axis in Figure 2) for their propagation, despite being on the same crack plane. Cracks on these planes advance at lower loading for a ⟨110⟩ crack front than for ⟨100⟩. Further, the atomistic simulations in the same study were in excellent agreement with the experiments [60]. Later these observations were also confirmed by several other atomistic works [27, 61, 62, 63, 64]. The consensus from all these studies was that the crack front dependence of crack growth originates from the discrete

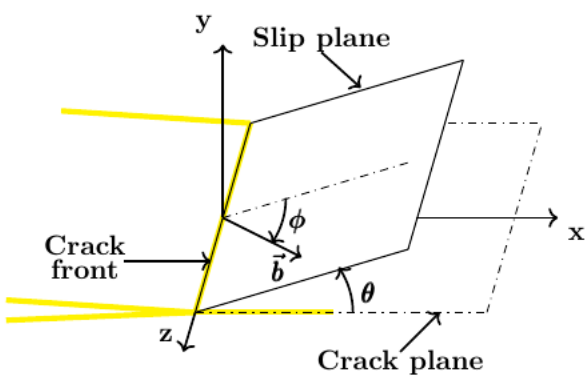

Figure 2: Orientation of slip system with respect to crack system. Here, $x-$ and $z-$ axes are the directions of crack propagation and front, respectively. $\vec{b}$ is the slip direction.

nature of atomic systems. In systems as such, an atomically sharp brittle crack does not grow continuously, but rather elongates and creates new surfaces via the sequential breaking of discrete atomic bonds [47]. Consequently, the crack can remain stable without propagating until an upper limit K_+ is reached during loading. The K_+ is generally observed to be higher than K_{IG} estimated using the Griffith model. Upon unloading, the same crack starts to close at a lower limit K_- which is lower than K_{IG}. The cause of these inequalities is that Griffith's theory does not take into account the discrete nature of atomic crack systems [47, 65]. Such behaviour of a crack is referred to as lattice trapping [47, 48]. The lattice trapping, which is termed bond trapping in the case of GB cracks, is quantified as ΔK given by [47, 48]

$$\Delta K = \frac{K_+}{K_-} - 1. \tag{12}$$

The crack front anisotropy reported in the literature is believed to be induced by lattice trapping, as the latter can vary depending on the crack front direction [60, 61, 66, 67, 68, 69].

2.2.2 Plastic crack-tip mechanisms

The plastic mechanisms at a crack-tip are dislocation emission and deformation twin formation. Crack-tip plasticity can be described with the help of Rice's theory [49, 50]. According to this theory, the stress intensity factor K_{IE} required exclusively for dislocation emission from a crack-tip is given by

$$K_{IE} = \sqrt{\frac{G_{IE}}{B}}, \tag{13}$$

where

$$G_{IE} = 8\frac{1 + (1 - \nu_{yx})\tan^2\phi}{(1 + \cos\theta)\sin^2\theta}\gamma_{us}. \tag{14}$$

Here, the material property γ_{us} is the unstable stacking fault energy of the concerned slip system. It is the energy barrier associated with the translation of one block of the material over the other (on the slip plane) in the slip direction, $\vec{b}$, until the total translation is equal to $|\vec{b}|$, as schematically shown in Figure 3(a). In body centered cubic (BCC) materials, such slip can occur on the slip planes [70]: {110}, {112} and {123} with $\vec{b} = \frac{a}{2}\langle 11\bar{1}\rangle$, where a, the lattice parameter, is measured at atomic level. A typical generalized stacking fault energy (GSFE) curve for a BCC material is provided in Figure 3(b). The angles θ and ϕ of equation (14) indicate the orientation of the slip system with respect to the crack plane, see Figure 2, while ν_{yx} is the Poisson's ratio.

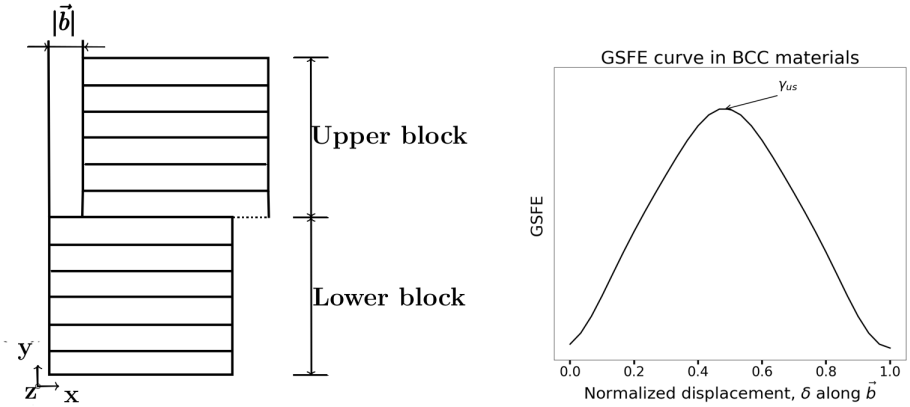

(a) (b)

Figure 3: (a) Schematics of GSFE and (b) Typical GSFE curve for BCC materials. Here, slip direction ($\vec{b}$) and slip plane normal are along the $x-$ and $y-$axes.

Likewise, the theoretical stress intensity factor, K_{IT}, responsible for the nucleation of a deformation twin at a crack-tip was estimated by Tadmor et al. [71, 72]. They introduced and computed a quantity called twinnability, T, for the qualitative assessment of deformation twin formation tendency in BCC and face centered cubic materials. It is given as

$$T = \Gamma_{crit}\sqrt{\frac{\gamma_{us}}{\gamma_{ut}}}, \tag{15}$$

where the unstable twin energy, γ_{ut}, is another material specific quantity associated with the twinning plane and slip system. It can be evaluated by sequentially shearing parallel twin planes ((112) in case of BCC) up to a total shear equal to the magnitude of the partial dislocation $\vec{b}_p$ ($= \frac{a}{6}[11\bar{1}]$ for BCC), see Figure 4. The factor Γ_{crit} is the normalized nucleation load [71], which is equal to unity for BCC materials [49, 50]. Then twin nucleation from a crack-tip is possible at K_{IT} evaluated as

$$K_{IT} = \frac{K_{IE}}{T} = \frac{K_{IE}}{\Gamma_{crit}}\sqrt{\frac{\gamma_{ut}}{\gamma_{us}}}. \tag{16}$$

This means that twin nucleation takes place at a crack-tip if T is higher than unity. Finally, the stress intensity factor K_{pl} at which either of the plasticity events, twinning or dislocation nucleation takes place, is defined as,

$$K_{pl} = \min(K_{IE}, K_{IT}). \tag{17}$$

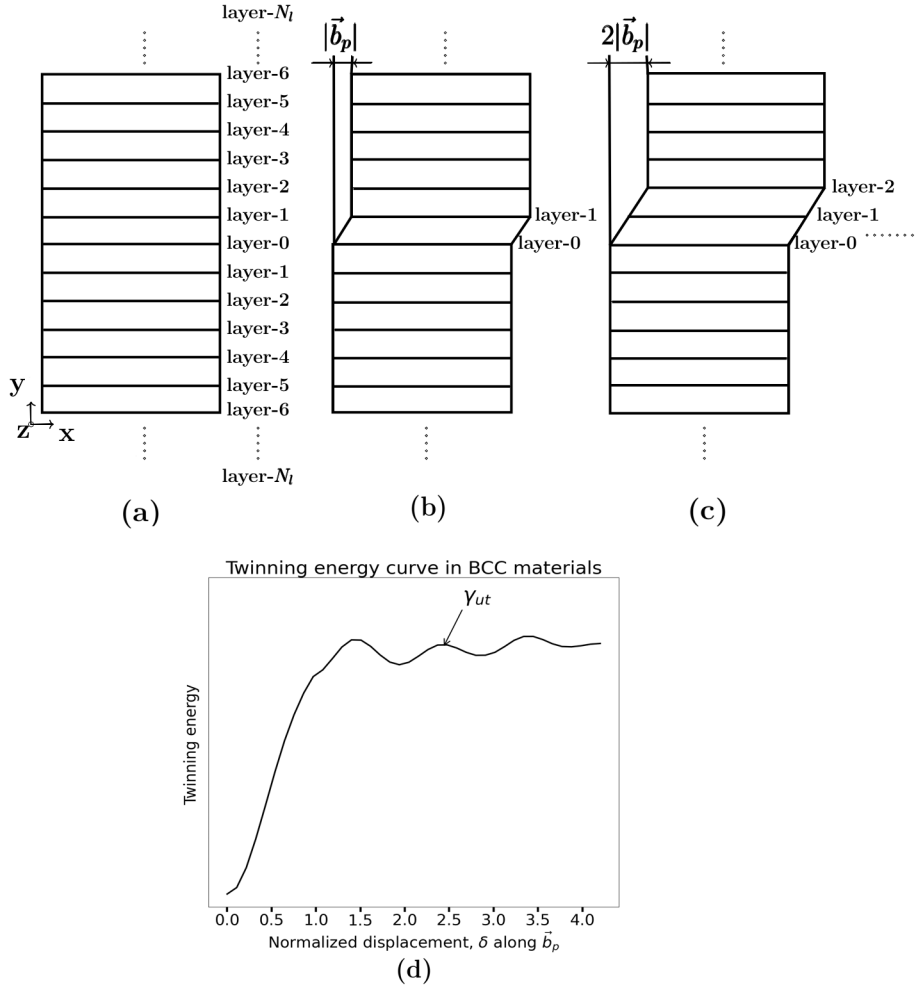

Figure 4: (a)-(c) Schematics of twinning. (d) Typical twinning energy pathway for BCC materials. Here, slip direction ($\vec{b}_p$) and slip plane normal are along the $x-$ and $y-$axes, respectively.

Analogous to the twinning tendency, another parameter called the tendency for plastic deformation, T_{pl}, can be evaluated as [61, 62, 63]

$$T_{pl} = \frac{K_{pl}}{K_{IG}}. \tag{18}$$

This is an indicator for the competition between brittle and plastic mechanisms, where $T_{pl} < 1$ suggests plastic mechanisms at the crack-tip, whereas brittle fracture can take place for $T_{pl} > 1$.

3 Grain boundaries

Ubiquitous in polycrystals, GBs are the atomic regions representing the transition from one grain of a specific crystallographic orientation into another of a different crystallographic orientation. Under deformation loading, material defects like dislocations and impurities diffuse into the GBs. Cracks in brittle materials preferably propagate along the GBs [25, 73]. Therefore, these planar defects are important parts of the microstructure and influence the deformation behaviour in polycrystals.

In general, a GB can be characterized by five macroscopic and three microscopic degrees of freedom (DOFs). The macroscopic DOFs can be chosen using different approaches [73, 74, 75]. For instance, the GB plane normal $\mathbf{n}_{GB}$ can be described using two DOFs. Then to match the orientation of a grain with that of the neighbour, the former needs to be rotated about an axis $\boldsymbol{R}$ (requires two DOFs and is also called misorientation/rotation axis) and an angle Θ (i.e. one DOF, also known as misorientation/tilt angle) [74]. Thus, two DOFs specify a GB plane and three DOFs are required to define the misorientation between the two grains, totalling to five macroscopic DOFs [73, 76]. Equivalently, the five macroscopic DOFs can be identified using a GB plane as the focus [76, 77, 78]. Two DOFs for each of the GB plane normals $\mathbf{n}_{GB}^{(1)}$ and $\mathbf{n}_{GB}^{(2)}$ in the two grains and a rotation angle Φ (one DOF, also known as twist angle) between the grains around the GB plane normal [76].

In order to obtain the equilibrium (or ground state) atomic configuration of a GB, one grain needs to be rigidly translated with respect to the other. As a result, three microscopic DOFs correspond to the translations. The microscopic DOFs are dependent on conditions like temperature, pressure and chemical composition of a GB, and need to be optimized to reach its ground state atomic configuration [76]. In atomistic simulations, these microscopic DOFs are typically optimized using the $\gamma-$surface approach [26, 79, 80]. This approach involves tracking the GB energy during translations of one grain in the GB plane relative to the other, while allowing the atoms to relax in the direction of the GB plane normal, post every increment of the translation. The GB energy is calculated as

$$\gamma_{GB} = \frac{E_{GB} - N_{GB} \cdot E_c}{2A_{GB}}. \tag{19}$$

In equation (19), the total energy of the N_{GB} atoms simulation cell containing the GB is represented by E_{GB} and A_{GB} is the projected GB area. E_c is the cohesive energy and the factor of two in the denominator accounts for the two GBs usually present in a periodic simulation cell. Ultimately, the configuration

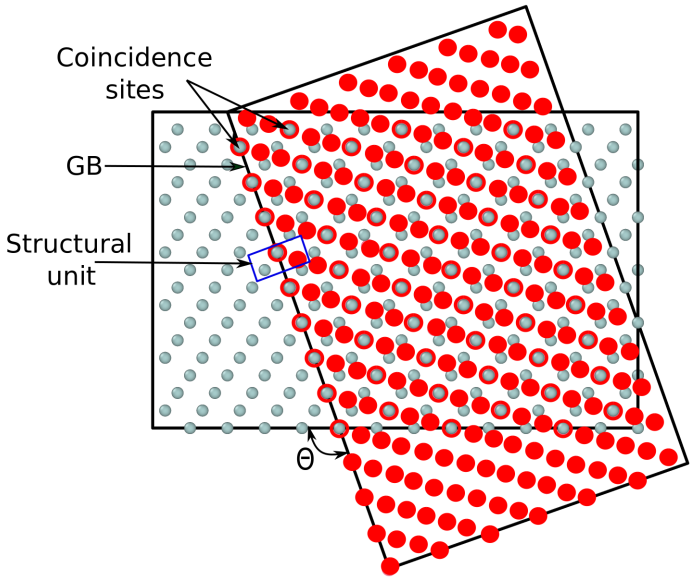

Figure 5: This figure illustrates a CSL with Σ3. One of the three sites in the structural unit is a coincidence site (equation (20)). Gray and red atoms belong to lattices before and after rotation by an angle Θ. The gray atoms with red background are coincidence lattice sites.

with the lowest γ_{GB} is the equilibrium ground state configuration of the GB whose microscopic DOFs are optimized.

To identify special GBs, Kronberg and Wilson [81] proposed the CSL model. The CSL model is based on the idea that overlaying a grain onto another generates a new lattice where there could be an overlap of one or more lattice sites from both grains. Such overlapping sites are termed coincidence sites, see Figure 5. Subject to the number of coincidence sites, a parameter Σ can be assigned to GBs. It is defined as

$$\Sigma = \frac{\text{Total number of sites in the unit cell of a CSL}}{\text{Number of coincidence sites in the CSL}}, \tag{20}$$

and can be interpreted as the degree of lattice equivalence of the two grains. The CSL model assumes that the presence of coincidence sites at the GB implies less distortion and that fewer bonds across the GB are broken and the GB energy is lower [82]. This is also indicative of lower entropy and in turn reduced Gibbs free energy [74]. Consequently, CSL GBs tend to exhibit high cohesion, low diffusivity and/or high conductivity [73], making them quite interesting.

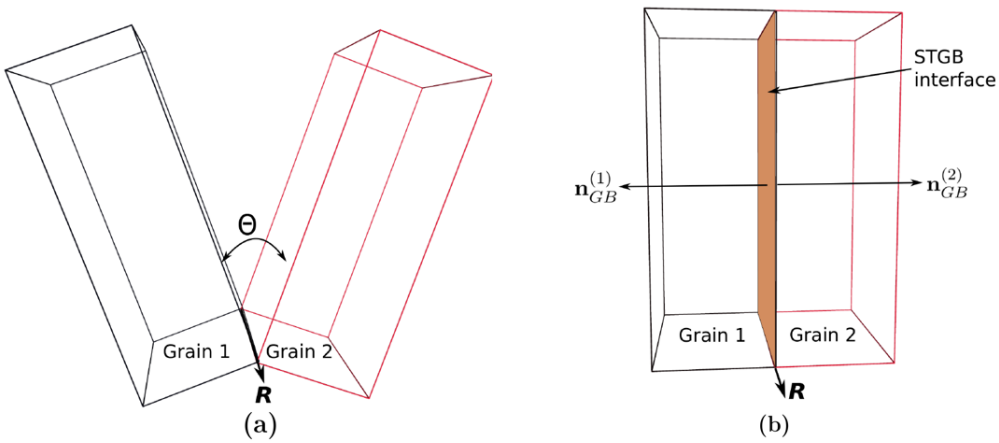

Figure 6: Illustration of STGBs. (a) Two symmetric grains with angle Θ between them and (b) STGB due to grains rotated equally about $\boldsymbol{R}$.

The symmetric tilt GBs (STGBs), which are a major part of the current work, constitute a special type of CSL GBs, see Figure 6. The two grains that are rotated by a misorientation angle Θ about a rotation axis $\boldsymbol{R}$ to form a STGB, possess mirror symmetry, i.e. $\mathbf{n}_{GB}^{(1)} = -\mathbf{n}_{GB}^{(2)}$. Additionally, there is no in-plane (GB plane) rotation angle, i.e. the twist angle, Φ, is zero. Thus, only two macroscopic DOFs are required for STGBs [73, 74]. Like in STGBs, the

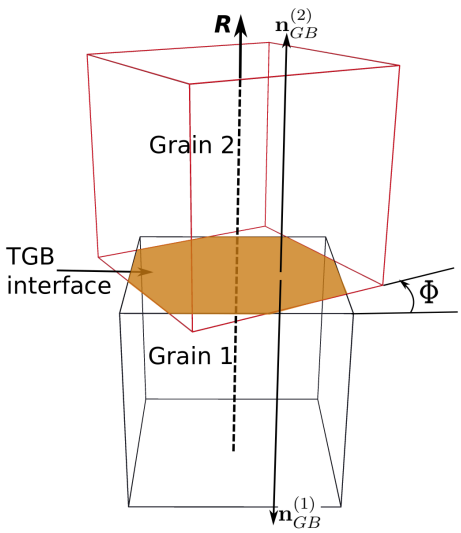

Figure 7: Illustration of TGBs. Only grain 2 is rotated about $\boldsymbol{R}$, thus creating a twist-like motion. The angle Φ is the twist angle.

normals of twist GBs (TGBs), $\mathbf{n}_{GB}^{(1)}$ and $\mathbf{n}_{GB}^{(2)}$, show mirror symmetry, see Figure 7. However, $\Theta = 0$ and $\Phi \neq 0$, and hence three DOFs for TGBs are needed [73, 74].

Using the information on DOFs and $\Sigma-$value, both STGBs and TGBs can be represented by using the notation $\Sigma Z(hkl)[uvw]$. Here, Z is the value of Σ of the GB. (hkl) and $[uvw]$ are the Miller indices of the GB plane and the misorientation axis, respectively.

4 Computational methods

First-principles methods such as DFT describe an atomic system exceptionally well, down to the ground states of electrons. These methods are based on quantum mechanical approximations and are generally computationally quite expensive to study atomic system dynamics or evolution. According to the Born-Oppenheimer (BO) approximation [83, 84], the time scale of electrons attaining ground state is minuscule compared to that of updating positions of nuclei. To investigate the dynamics of a system, *ab initio* MD simulations rely on the BO approximation. They solve the equations of motion for the nuclei alone using the atomic forces computed from electronic ground states. When the nuclei occupy new positions, the forces are updated through electronic ground state structure calculations [84]. Despite the superiority over DFT in terms of computational speed, *ab inito* MD cannot capture the fracture mechanisms due to the time and length scales involved. Hence, classical atomistic simulations, which use empirical interatomic potentials, appear to be better positioned to study fracture.

4.1 Classical atomistic modelling

4.1.1 Molecular statics

In MS simulations, there is no time evolution of the system of interacting atoms and the atomic structures are relaxed. This is achieved by using various types of optimization algorithms, see e.g. [85]. The potential energy of an atomic system is given by an interatomic potential, whose format depends on the species of the interacting atoms. If E_{pot} is the energy functional approximating the non-convex potential energy landscape, with stable and metastable atomic configurations, the optimization algorithms search for configurations for which the potential

energy is at a local minimum. In conservative systems, the force ($\vec{f_i}$) on an atom positioned at $\vec{r_i}$ can be obtained as

$$\vec{f_i} = -\frac{\partial E_{pot}}{\partial \vec{r_i}}. \tag{21}$$

For a minimum potential energy configuration, i.e. a stable or metastable equilibrium configuration, the forces are zero. Therefore, an optimization algorithm searches for equilibrium configurations, by minimizing an objective function. The objective function typically relies on force and energy convergence criteria, such that a configuration is considered as an equilibrium configuration if the change in potential energy, ΔE_{pot}, and force vector, are less than a prescribed energy and force tolerance, respectively. Accordingly, there is no time scale in MS simulations.

Even though a system does not evolve dynamically in MS simulations, quasi-static simulations in which a system undergoes spatial evolution very slowly can be performed in MS settings. This allows the computation of certain material properties e.g. elastic constants for which time scaling is not a necessity. However, MS simulations do not consider temperature, because the kinetic energy gets dissipated during the search for local potential energy minimum [86, 85]. Consequently, MD simulations are necessary to study materials at finite temperatures.

4.1.2 Molecular dynamics

Based on Newtonian mechanics, the governing equation for the temporal evolution of a system in MD simulation is Newton's second law of motion. Thus, the force on the i^{th} atom of mass m_i in the system can be expressed as,

$$\vec{f_i} = m_i \ddot{\vec{r}}_i \tag{22}$$

The spatial and temporal evolution of an atomic system can be tracked by solving the second-order differential equation (22), which is a many-body problem. This is realized numerically by using time integration schemes in MD simulations. The scheme chosen for this purpose should be stable and conserve the total Hamiltonian of an isolated system [87, 88]. Furthermore, the timestep chosen in the integration schemes should be small enough to accurately capture the atomic thermal vibrations [87]. Therefore, typical MD timestep values are in the order of femtoseconds. Accordingly, simulation of processes that occur at a higher timescale is quite expensive even with today's powerful high-performance

computers. The solution to the problem of the computational cost of such simulations is sought in statistical mechanics [87].

An atomic system has very many possible arrangements of all the particles representing different points in the configuration space. These arrangements constitute microscopic DOFs of the system. According to classical statistical mechanics, a very large number of the microscopic DOFs correspond to the same thermodynamic state of an isolated system in equilibrium [87, 89]. Therefore, one can have a very large number of replicas of the original system that only differ at the microscopic level and are equivalent to each other at the macroscopic level [87, 89]. A collection of all such replicas of the original system forms a statistical ensemble and thermodynamic quantities are averaged over all the replicas yielding an ensemble average. According to the ergodicity hypothesis, when the system is allowed to dynamically evolve for a sufficiently long enough time, it passes through all the accessible microscopic DOFs yielding the time average of thermodynamic quantities equal to their ensemble average [87, 89]. Systems that obey this hypothesis are ergodic. Thus, the macroscopic quantities such as temperature, pressure, energy etc. at atomistic scale are related to the time averages in MD [87].

Contingent on the nature of the MD simulation, statistical ensembles such as the microcanonical (NVE), the canonical (isochoric-isothermal or NVT) or the isobaric-isothermal (NPT) ensemble can be used. Besides keeping the number of particles (N) constant, the microcanonical ensemble is associated with constant total energy, E, and volume, V, of the system, and follows Newtonian dynamics. In the canonical ensemble, the simulations are isothermal with constant T, instead of constant E. The isobaric-isothermal ensemble deals with maintaining a constant average pressure, P, while a constant temperature, T, is sustained. The temperature is linked to the time average of total kinetic energy E_{kin} via the following relation [87]

$$T = \frac{2}{3}\frac{\langle E_{kin} \rangle}{N k_B} = \frac{1}{3 N k_B}\left\langle \sum_{i}^{N} m_i v_i^2 \right\rangle \tag{23}$$

where m_i and v_i are the mass and velocity of atom i, respectively, and the brackets indicate the time averaging. The parameter k_B is the Boltzmann constant. Along the same lines, pressure can be evaluated as the time average of the Virial stresses [90, 91] and is given by [87]

$$P = \left\langle -\frac{1}{V}\sum_{i=1}^{N}\left[m_i v_i^{\alpha} v_i^{\beta} + \sum_{j \neq i}^{N} F_{ij}^{\alpha} r_{ij}^{\beta} \right] \right\rangle. \tag{24}$$

Here, the force between the i^{th} and j^{th} atoms, separated by a distance r_{ij}, is F_{ij}^{α}. m_i and v_i^{α} stand for the atomic mass and velocity vector of the i^{th}-atom, respectively.

Finite temperature MD simulations within the NVT ensemble can be realized by maintaining a constant temperature using a thermostat, e.g. Andersen [92], Berendsen [93], Langevin [94, 95] or Nosé-Hoover thermostats [96, 97, 98, 99]. Using a thermostat includes coupling the system to a heat reservoir. In this work, the Nosé-Hoover thermostat, which is a deterministic approach possessing time-reversibility, is employed to maintain the system at constant T. It is based on the extended Lagrangian of a system. The extended system comprises additional DOFs to those of the original system. The equations of motion derived from this extended Lagrangian contain a damping term enabling the heat exchange with a heat reservoir such that the system is maintained at the desired temperature [87]. Likewise, the pressure in an NPT ensemble can be maintained using a Nosé-Hoover barostat, which is based on the extended Hamiltonian [87].

4.1.3 Atomistic Monte Carlo modelling

Studying the time evolution (dynamics) of atomic systems using deterministic equations of motion may in some situations become a computational bottleneck. For example, in finding equilibrium positions for impurities in a host, which is a frequently performed task in this study. Equilibration of such systems and evaluation of the previously mentioned statistical ensemble/time averages of thermodynamic quantities can also be realized using Monte Carlo (MC) simulations. A MC simulation achieves this by adopting a stochastic sampling approach that entails probing only the statistically important areas of the configuration space [87]. The statistically important regions are those with configurations corresponding to the Boltzmann distribution. Consequently, MC simulations use different sampling algorithms in a variety of ensembles, including those that are only feasible in MC simulations, e.g. grand canonical, semi-grand canonical and Gibbs ensembles [87].

The algorithm developed by Metropolis et al. [100] is a popular algorithm for sampling. The algorithm can be outlined as [87, 100]

- Randomly select a configuration.
- The energy $E(\boldsymbol{r})$, where $\boldsymbol{r}$ contains position vectors of all the atoms in the system, is calculated for the selected configuration.

- A new configuration is generated by displacing one or more atoms chosen at random in the current configuration.
- Calculate the energy $E(\boldsymbol{r}^{New})$ for the new configuration and the change in energy, $\Delta E = E(\boldsymbol{r}^{New}) - E(\boldsymbol{r})$.
- The new configuration (arrangement of atoms $\boldsymbol{r}^{New}$) is accepted with probability, $P_{acc}(\boldsymbol{r} \rightarrow \boldsymbol{r}^{New})$ given by,

$$P_{acc}(\boldsymbol{r} \rightarrow \boldsymbol{r}^{New}) = \min\Big(1, \exp\Big(-\beta \Delta E\Big)\Big). \tag{25}$$

Here, $\beta = 1/k_B T$. The above steps are iterated for a certain number of steps. In equation (25), the probability of sampling a specific configuration is proportional to the Boltzmann factor exp(-$\beta\Delta E$), thus enabling sampling of only statistically important configurations. In this study, MC simulations with the Metropolis algorithm [100] were used in Papers II-IV to swap P and W atoms such that the impurity segregation at equilibrium sites at GBs could be obtained.

4.2 Interatomic potentials

One of the most essential ingredients for classical atomistic modelling is the interatomic potential, which describes how atoms interact with each other. The simplest type of interatomic potential formalism is a pair potential. In this formalism, the total potential energy of an atomic system is computed as the sum of interactions between pairs of atoms. These pair potentials can satisfactorily describe ionic materials where there are only Coulomb interactions (attractions and repulsions), and noble gases [101, 102]. However, they are not suitable for metallic crystals where the atomic interactions are beyond just pair-wise [88]. For instance, pair potentials predict $C_{12} = C_{44}$ in the elasticity tensor i.e. the Cauchy relation is satisfied, which is contrary to what is observed in most cubic metals [101, 102]. Furthermore, vacancy formation energy is systematically overestimated [101, 102]. These shortcomings led to the development of alternatives. The most popular semi-empirical interatomic potentials used to describe and study metallic systems are of many-body central force formalisms, for example, the embedded atom method (EAM) [101, 102, 103, 104] and its extension - the modified embedded atom method with second nearest-neighbour interactions (2NN-MEAM) included [105, 106]. This section provides a brief introduction to the EAM and 2NN-MEAM formalisms.

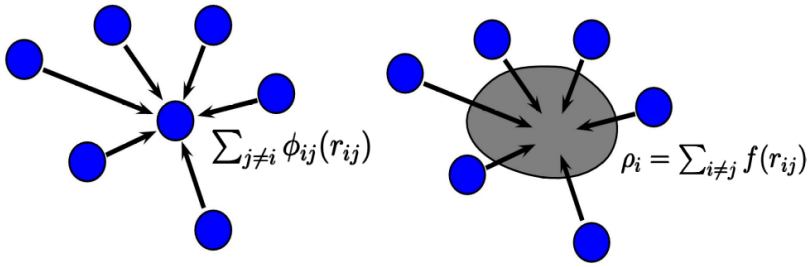

Figure 8: Illustration of pair-wise term and background electron density in the EAM formalism.

4.2.1 Embedded atom method potentials

EAM potentials [101, 102, 103, 104] involve an extension of pair potentials, which entails the addition of an embedding energy term to account for the metallic cohesion. The potentials based on the EAM model are well-established to study the deformation of metals. The potentials are generally fitted to experimental and/or *ab inito* materials properties databases that are application specific [107].

According to this formalism, the total potential energy consists of contributions from (i) the screened pair-wise Coulomb interactions and (ii) the energy required to embed an atom in the background of electrons with density, ρ_i, see Figure 8. Thus, the functional form of the total potential energy for a configuration of N atoms is defined as [101, 102, 103, 104],

$$E_{pot} = \frac{1}{2}\sum_{i}^{N}\sum_{j\neq i}^{N}\phi_{ij}(r_{ij}) + \sum_{i}^{N}F_i(\rho_i) \tag{26}$$

where $F_i(\rho_i)$ is the embedding energy of atom i in the background electron density ρ_i at the site of the same atom. The background electron density is computed as a linear superposition of contributions from the neighbouring atoms,

$$\rho_i = \sum_{i\neq j} f(r_{ij}) \tag{27}$$

such that ρ_i is a function of r_{ij}, called the transfer function, $f(r_{ij})$. The many-body embedding energy term accounts for all the interactions between atom i and its neighbouring atoms. The function $\phi_{ij}(r_{ij})$ is a pair-wise interaction energy term between atoms i and j. Generally, $\phi_{ij}(r_{ij})$ and $f(r_{ij})$ are often approximated by polynomial functions with parameters that can be fitted to a materials properties database. For both the pair-wise and embedding energy,

the number of neighbouring atoms considered is restricted by the cutoff radius, r_c, beyond which the interactions are neglected. The choice of r_c affects the speed of the atomistic simulation and the computed material properties. From equations (26) and (27), it can be realized that the EAM potentials are spherically symmetric, which makes them popular potentials primarily for close-packed metals with completely filled $d-$orbitals, but they exist also for others, such as BCC metals.

4.2.2 Modified embedded atom method potentials

Transition metals (such as W, iron etc.) in which the $d-$orbitals are partially filled, and materials with directional covalent bonding from $sp-$bonding orbitals, exhibit angular dependencies. Additionally, angular dependencies of the potential energy are also obvious at locations of defects. To capture these effects, Baskes [108] proposed an extension of the EAM, the modified embedded atom method (MEAM) by including an angular dependent embedding energy term, which only included the first-nearest neighbours. Later, it was extended by Lee and Baskes [105, 106] into the 2NN-MEAM, which also includes second-nearest neighbour interactions. By including second-nearest neighbour interactions, the potentials predict material properties even more accurately than when only first-nearest neighbour interactions are taken into account. Because MEAM includes angular dependencies, it is more suitable for BCC metals and semiconductors than EAM [108, 109].

In the 2NN-MEAM framework, the total potential energy of an atomic configuration is given by [105, 106]

$$E_{pot} = \frac{1}{2}\sum_{i}^{N}\sum_{j\neq i}^{N} S_{ij}\phi_{ij}(r_{ij}) + \sum_{i}^{N} F_i(\bar{\rho}_i) \tag{28}$$

where

$$S_{ij} = \prod_{k\neq i,j=1} S_{ikj} \tag{29}$$

and

$$F_i(\bar{\rho}_i) = AE_c(\bar{\rho}_i/\bar{\rho}_0)\ln(\bar{\rho}_i/\bar{\rho}_0). \tag{30}$$

Here, S_{ij} is the pairwise screening function that represents the screening of the pair interaction energy $\phi_{ij}(r_{ij})$ between atoms i and j. It is the product of all partial screening contributions, S_{ikj}, which emerge from the interaction with the remaining atoms, k. The partial screening is computed based on the

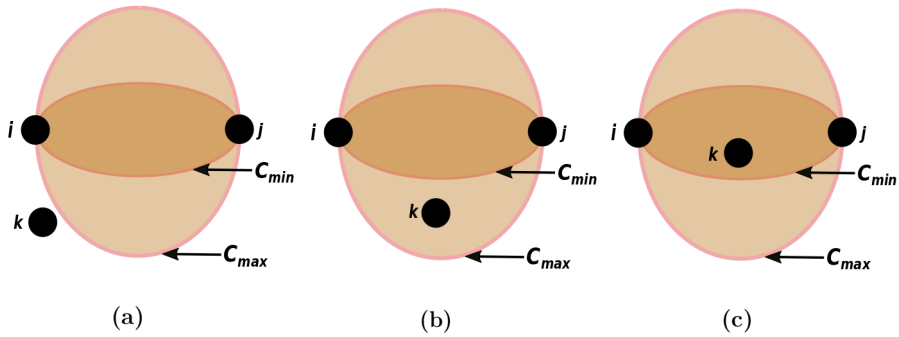

Figure 9: Illustration of the screening parameter S_{ikj}. The atom k placed (a) outside the outer ellipse yields no screening, i.e. $S_{ikj} = 1$, (b) between inner and outer ellipse yields partial screening, i.e. $0 < S_{ikj} < 1$, and (c) inside the inner ellipse yields full screening, i.e. $S_{ikj} = 0$.

construction of an inner and an outer ellipse, as shown in Figure 9. The equation of such an ellipse is given by [105, 106]

$$x^2 + \frac{y^2}{C} = \left(\frac{r_{ij}}{2}\right)^2 \tag{31}$$

Here, for atom k, C is obtained based on the relative distance between atoms i, j and k, and is unique to an ellipse with a unique $y-$axis. Then for values C_{max} and C_{min}, we will have ellipses as shown in Figure 9. In the case of an ellipse corresponding to a value C obtained for an atom k that screens the $\phi(r_{ij})$ between atoms i and j, we get S_{ikj} in terms of a smoothening function f_c as [105, 106]

$$S_{ikj} = f_c\left(\frac{C - C_{min}}{C_{max} - C_{min}}\right). \tag{32}$$

When $C > C_{max}$, the atom k is outside the ellipse for C_{max} and has no screening effect on $\phi(r_{ij})$, meaning S_{ikj} must be unity, see Figure 9(a). Similarly, for $C_{min} \leq C \leq C_{max}$, f_c takes the form [105, 106]

$$f_c\left(\frac{C - C_{min}}{C_{max} - C_{min}}\right) = \left\{1 - \left(1 - \left[\frac{C - C_{min}}{C_{max} - C_{min}}\right]^4\right)\right\}^2 \tag{33}$$

such that $0 < S_{ikj} < 1$, which represents partial screening, see Figure 9(b). Then, if $C < C_{min}$, atom k completely screens the $\phi(r_{ij})$, yielding $S_{ikj} = 0$, see Figure 9(c). Thus, through S_{ikj} the extent of screening of $\phi(r_{ij})$ by an atom k can be quantified.

For the embedding energy in equation (30), $\bar{\rho}_i$ is the background electron density and A is a fitting parameter. The background electron density in the reference structure is represented by $\bar{\rho}_0$. Of the different flavors of 2NN-MEAM, the following is the description of $\bar{\rho}_i$ as provided in [110] and is that adopted in the current work. Here, $\bar{\rho}_i$ is given by

$$\bar{\rho}_i = \sum_{h=1}^{3} t^{(h)} [\rho_i^{(h)} / \rho_i^{(0)}]^2 \tag{34}$$

where $h = 0$, 1, 2 and 3 can be thought of as representing s, p, d and f orbitals, respectively. The weight parameters $t^{(h)}$ control the contribution of partial electron density $\rho_i^{(h)}$, relative to the atomic site i dependent reference density, $\rho_i^{(0)}$, to the total background electron density at the site of atom i. As a consequence, the angular dependencies mentioned previously are accounted for in the 2NN-MEAM formalism via the density term. The partial electron densities are calculated as [110]

$$\rho_i^{(0)} = \sum_{j \neq i} f_j^{(0)}(r_{ij}) \tag{35}$$

$$\rho_i^{(1)} = \left[\sum_{\alpha} \left[\sum_{j \neq i} f_j^{(1)}(r_{ij}) \frac{r_{ij}^{\alpha}}{r_{ij}} \right]^2 \right]^{1/2} \tag{36}$$

$$\rho_i^{(2)} = \left[\sum_{\alpha,\beta} \left[\sum_{j \neq i} f_j^{(2)}(r_{ij}) \frac{r_{ij}^{\alpha} r_{ij}^{\beta}}{r_{ij}^2} \right]^2 - \frac{1}{3} \left[\sum_{j \neq i} f_j^{(2)}(r_{ij}) \right]^2 \right]^{1/2} \tag{37}$$

$$\rho_i^{(3)} = \left[\sum_{\alpha,\beta,\gamma} \left[\sum_{j \neq i} f_j^{(3)}(r_{ij}) \frac{r_{ij}^{\alpha} r_{ij}^{\beta} r_{ij}^{\gamma}}{r_{ij}^3} \right]^2 \right]^{1/2} \tag{38}$$

where α, β and γ are the coordinate axes. The radial functions $f_j^{(h=0,1,2,3)}$ are pair-wise electron density functions given by

$$f_j^{(h)}(r_{ij}) = \rho_0 \exp[-\beta^{(h)}(r_{ij}/r_e - 1)], \tag{39}$$

where the quantities ρ_0 and $\beta^{(h)}$ are fitting parameters. The parameter r_e represents the nearest neighbour distance in the reference structure. For a two component (atomic species) system, the mixed background electron density in equation (34) becomes [106],

$$\bar{\rho}_i^{binary} = \frac{2\rho_i^{(0)}}{1 + \exp[-\sum_{h=1}^{3} t^{(h)} [\rho_i^{(h)} / \rho_i^{(0)}]^2]} \tag{40}$$

and $f_j^{(h)}(r_{ij})$ in equation (39) is computed using standard averaging.

For a single component system, the 2NN-MEAM formalism returns the EAM formalism if $t^{(1)} = t^{(2)} = t^{(3)} = 0$ [110]. In terms of computational efficiency, EAM potentials are typically faster than 2NN-MEAM, but the latter provides an improved basis to describe the cohesion of BCC metals.

4.3 Atomistic fracture modelling

At the atomic length scale, the energetics of crack planes can be obtained using electronic methods based on quantum mechanical approximations, such as DFT. It relies on computing the decohesion energetics associated with rigid or relaxed separation of planes onto which a crack is prescribed to propagate [26, 39, 40, 42]. This indicates that prior knowledge of the crack propagation path is essential, when in actuality the path of a crack may not be so well defined or perceived in advance. This is a limitation of DFT based fracture modelling.

Due to the reduced computational cost and the possibility to study larger systems, classical atomistic fracture simulations are preferred. They do not necessitate the specification of crack planes beforehand and can facilitate unconstrained crack extension along energetically preferable paths. They are quite suitable for the understanding of crack-tip processes responsible for brittle to ductile transition (BDT) in materials [111]. This implies that the role of impurities in such BDT is also accessible. But, care must be taken to choose an appropriate atomistic setup since the behaviour of a crack is influenced by a wide range of factors such as crack geometry, applied boundary conditions, type of loading i.e. quasi-static or dynamic, and strain rate in dynamic loading simulations [63].

The most commonly used crack models in the literature for the atomistic fracture studies comprise quasi-2D cracks [111]. Cracks of this sort in pristine materials have straight fronts where all the atomic bonds along the crack front are broken simultaneously upon critical loading [111]. Typically, these cracks are used as a center or edge crack in atomistic simulations, as was the case in [63]. As implied by the name, a center crack is situated at the center and an edge crack at the edge of the crack geometry. Being bound inside the specimen, the center crack is finite in size whereas the edge crack is semi-infinite.

The crack specimens in atomistic simulations are of the order of a few nanometers. As a consequence of this, local stress levels at and ahead of the crack-tip are very high at this length scale. The high local stresses cause the region around the crack-tip to behave non-linearly or inelastically [52]. This indicates that there exists a FPZ of radius R_{FPZ}. Therefore, the used crack geometry must

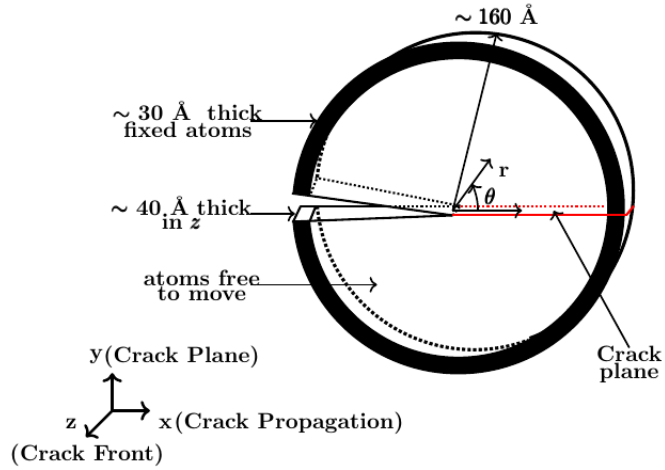

Figure 10: Crack simulation setup in 3D.

satisfy the small scale yielding condition, as mentioned in Section 2.1. Andric and Curtin [52] showed that the small-scale yielding condition is not satisfied by the finite size cracks, like center cracks, and hence they are not suitable for LEFM based fracture simulations. From the Dugdale model [112, 113], the typical size of the K_I-dominant region is 0.15 times the crack length [52]. Because of the essentially infinite length of the crack, a_{crack}, for a semi-infinite crack, such as an edge crack, the entire simulation cell becomes K_I-dominant. Further, for such cracks, the FPZ was found to be small in comparison with R_{K_I}, thus satisfying small-scale yielding condition [52]. The study by Shimada et al. [114], which relied on an energy release rate approach to determine the fracture toughness of semi-infinite cracks, also showed that LEFM does not break down at the length scale of atomistic fracture simulations.

Accordingly, the very well-established semi-infinite crack setup from the literature [38, 52, 61, 63, 115, 116] (see Figure 10) was used for the investigation of fracture in W in the current work. The quasi-static MS modelling of the cracks involved the application of mode-I K_I-controlled displacement fields from LEFM (equations (5) and (6)) to single- and bicrystal cracks under plane strain conditions. In Papers III and IV, for an energy release rate based evaluation of the fracture toughness and estimation of interfacial excess potentials of GBs containing impurities, the above setup was augmented to include cohesive zone volume elements (CZVEs) that constitute the cohesive zone of the GBs.

5 Summary of results

5.1 Paper I - Applicability of potentials for fracture studies

There are several interatomic potentials based on the EAM and 2NN-MEAM formalisms for W available in the literature [117]. Most of them were developed for applications such as radiation-induced damage studies [30, 118]. This necessitates the evaluation of their applicability for fracture studies. Accordingly, fracture-related properties and the crack-tip behaviours were evaluated for seven EAM potentials (denoted EAM-1 to EAM-7) [119, 120, 121, 122, 123, 124, 125], and two 2NN-MEAM potentials: MEAM-1 [106, 116] and MEAM-2, of which the latter was fitted as part of Paper I. This study aimed to identify suitable potentials that could serve as the basis for fitting of the binary W-P potential to be used in Papers II-IV.

The principal driver of the behaviour of a crack is the competition between brittle and plasticity mechanisms. Evaluation of the intrinsic plasticity-related properties (γ_{us} and γ_{ut}), revealed that the different potentials gave rise to widely different results, see Table 1. While the 2NN-MEAM potentials predicted data in good agreement, some of the EAM potentials were found to either severely overestimate or underestimate DFT data. The same tendencies were observed for properties related to brittle fracture ($\gamma_{(klm)}$ and γ_{GB}), which reflects the fact that empirical potentials have limited predictability outside the fitting database. Additionally, rigid traction-separation (TS) data was evaluated for selec-

Table 1: Performance of potentials in reproducing fracture related properties in comparison with corresponding DFT data. Here, "++", "+" and "–" refer to "consistent" (< 10% deviation), "partially consistent" (< 20% deviation) and "inconsistent" (> 20% deviation) behaviour, respectively. Also, "TS-B" and "mag" are short for smooth, positively skewed bell-shaped TS-behaviour and magnitude, respectively. Finally, "consistent with fracture experiments" refers to consistency of observed mechanisms with experiments.

	Bulk properties			**Single-crystal fracture**				**Bicrystal fracture**		
Potential	C_{ij}	$\gamma_{us,(110)}$	γ_{ut}	$\gamma_{(klm)}$-mag	$\sigma_{coh}^{(klm)}$	TS-B$_{(klm)}$	Consistent with fracture experiments	$\sigma_{coh,(GB)}$	TS-B$_{\mathrm{GB}}$	γ_{GB}
EAM-1	++	–	–	+	+	++	++	+	+	+
EAM-2	++	+	+	+	–	–	+	–	–	–
EAM-3	++	–	–	–	–	–	+	–	+	+
EAM-4	++	++	++	–	–	–	++	–	–	+
EAM-5	++	+	+	–	–	++	–	–	++	+
EAM-6	++	++	++	–	–	++	–	–	+	++
EAM-7	++	++	++	+	–	–	++	–	–	–
MEAM-1	++	++	+	+	++	++	++	+	++	++
MEAM-2	++	++	++	++	++	++	++	+	++	++

ted single-crystalline and GB cleavage planes to assess the potentials' ability to reproduce the corresponding DFT data. The outcome from this comparison revealed that several of the EAM potentials displayed traction-separation characteristics that did not concur with the DFT results. This included features such as multiple local maxima, negative stress regions or significant oscillatory behaviour. Moreover, the peak stresses were on most accounts too high, while the interaction range was found to be short.

In line with experimental results [19, 20, 60, 126, 127, 128, 129, 130, 131], which demonstrate the {100} and {110} to be the primary and secondary cleavage planes of W, most potentials exhibited a preference of cleavage for those planes in the fracture simulations using K_I-controlled loading setup. This manifested in general low fracture toughness associated with those crack planes. However, for a subset of the considered EAM potentials, cleavage was followed by crack-tip transformation, which is accepted to be an artifact and a shortcoming in terms of the potentials' applicability for fracture modelling. In the fracture simulations, in accordance with previous experimental and atomistic studies [27, 60, 61, 62, 63, 64], crack front dependencies were observed in the crack-tip behaviour. The {100} and {110} cracks preferred ⟨110⟩ crack-fronts. When evaluating the lattice and bond trapping, the EAM potentials were generally found to exhibit ΔK up to approximately one order of magnitude higher than the 2NN-MEAM potentials. This behaviour was found to correlate with features of the traction-separation curves, where potentials with short interaction range and high peak stress exhibit high trapping. Furthermore, the high lattice and bond trapping promoted plasticity behaviour at the crack-tip, despite the theoretical prediction of brittle fracture for $T_{pl} > 1$.

Based on this evaluation, which is summarized in Table 1, three potentials, MEAM-1, MEAM-2 and EAM-1, were identified as the most appropriate for fracture modelling. However, MEAM-1, whose predictability was comparable with that of MEAM-2, yielded an unphysical crack-tip behaviour (double - branching with localized crack-tip transformation) for a pristine STGB crack, which is believed to be an artifact. Accordingly, MEAM-2, which exhibited better agreement with DFT data for properties such as GSFE, twinning energy, surface and GB energies than EAM-1, and also reproduced traction-separation curves of the considered systems and crack-tip behaviours better, was chosen for the continued study.

5.2 Paper II - Impact of phosphorus impurities on grain boundary cohesion

In Paper II, the impact of P impurities on the cohesion of ⟨110⟩ STGBs was investigated by carrying out strain rate controlled classical MD tensile simulations at room temperature. For the simulations, a newly fitted 2NN-MEAM potential for the W-P binary system was employed. The study considered a low impurity coverage ($\theta \leq 0.02$ Å^{-2}, with θ defined as the number of impurities per GB area unit) and was conducted below the BDTT. It covered a large set of STGBs in the approximate misorientation angle range $10° < \Theta < 170°$.

For pristine GBs, the overall dominating mode of failure was found to be brittle cleavage. However, plastic mechanisms, which included dislocation emission and/or twin nucleation, accompanied by void formation were occasionally observed before the GB ultimately underwent brittle failure, see Figure 11(a)-(c). Notably, such behaviour was predominant among GBs with low misorientation angle ($\Theta < 44°$), but did also occur for occasional GBs in the remaining range of considered misorientation angles.

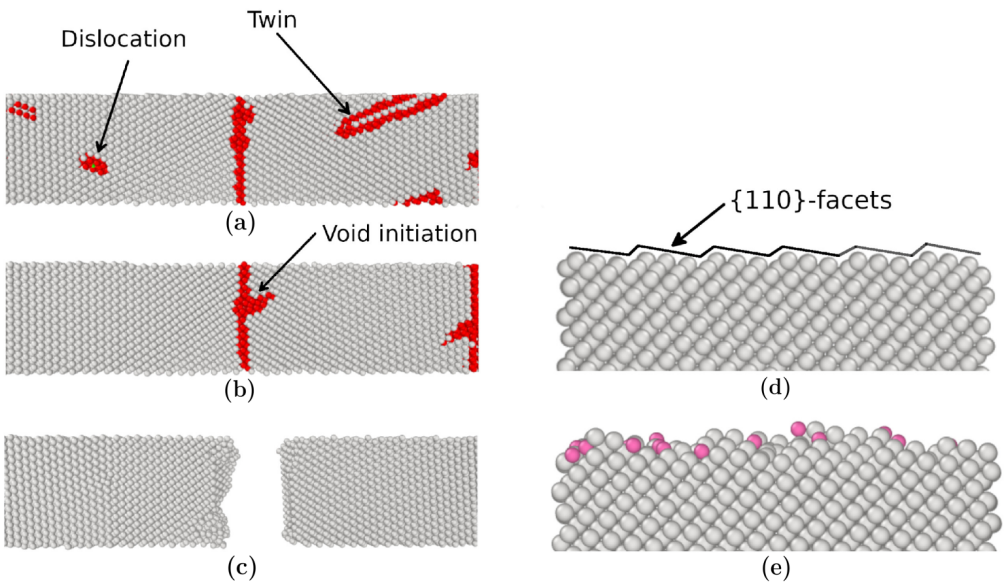

Figure 11: Dislocation, twinning, void and brittle (DTVB) failure events as observed in the pristine $\Sigma41(\bar{3}38)[110]$ GB: (a) Dislocation and twin nucleation, (b) void formation and (c) cleavage. Fracture surfaces for the $\Sigma43(\bar{3}35)[110]$ GB indicating (d) faceting for the pristine GB and (e) lack thereof for the impurity coverage $\theta = 0.02$ Å^{-2}.

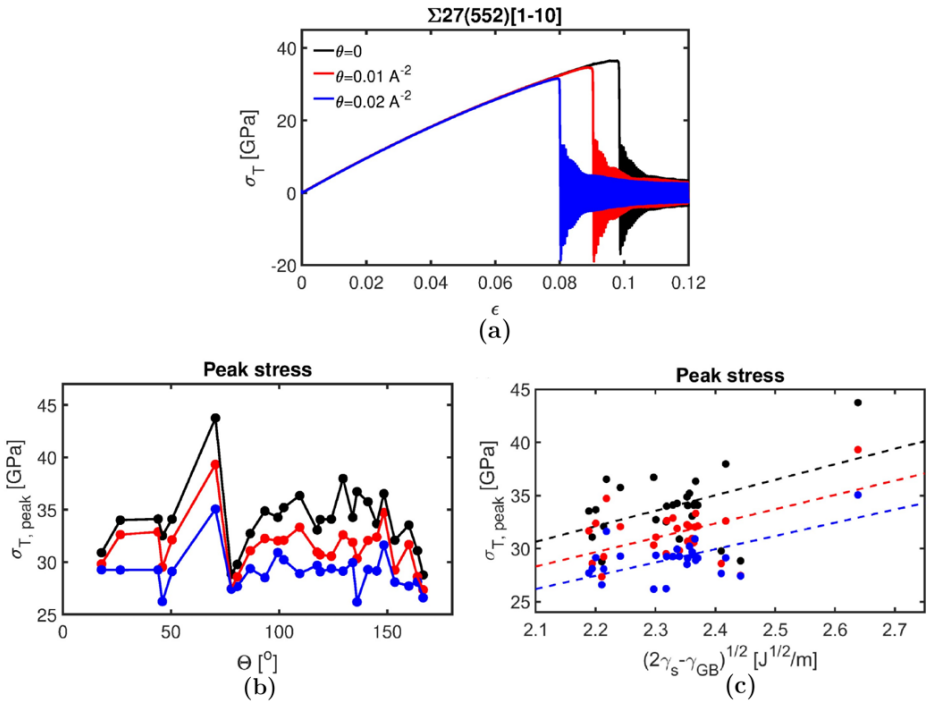

Figure 12: (a) Stress vs. strain curves for the $\Sigma27(552)[1\bar{1}0]$ GB for different degrees of impurity coverage. The post-cleavage oscillations are attributed to wave propagation that emerges as a result of recoiling upon failure. Effect of impurity coverage on the peak stress associated with brittle failure: (b) peak stress as function of misorientation angle and (c) as function of the ideal energy release rate. In (c) the dashed lines indicate a linear fit between the peak stress and the square root of the energy release rate.

For the GBs that were brittle in their pristine state, the introduction of impurities did not alter the observed failure mechanism. It did, however, affect the nature of the fracture planes. Most notably, for GBs with {110}-facetted fracture surfaces in their pristine form (see Figure 11(d)), disordered fractured surfaces decorated with impurities were noticed occasionally (see Figure 11(e)). Impurities would further contribute to the suppression of plastic mechanisms. This is indicative of the P impurities weakening the bonds between W atoms thereby reducing the cohesion strength of the GBs. This was verified by the evaluation of the stress-strain curves, which confirmed a reduced peak tensile stress for P segregated GBs for increased impurity coverage, see Figure 12, although to a varying degree for different GBs. Despite that the impurity content considered in this paper was less than observed experimentally, these results were indicative of P impurities contributing to GB embrittlement in W, which is in line with most experimental observations [25, 29].

5.3 Paper III - Impurity-induced embrittlement of symmetric tilt grain boundaries

Although the tensile simulations in Paper II substantiated the reduction in GB cohesion, the influence of the P impurities on the fracture toughness of the GB cracks was not revealed. This prompted the investigation of the impact of P impurities on the fracture behaviour of STGB cracks in Paper III. In this regard, the STGB cracks with varying P impurity concentrations were examined using the K_I-controlled crack setup that included CZVEs. From these simulations, the fracture toughness of the cracks was estimated via three approaches: using (i) the individual and (ii) the averaged energy release rate of CZVEs along the fractured surfaces in Griffith's model (denoted by K_{IC}^{CZ} and K_{IC}, respectively), and (iii) as the applied critical stress intensity factor at which a crack starts to propagate (denoted by K_{IC}^{R}). Thus, the three approaches exhibit varying levels of locality in the GB. The advantage of the first two approaches was that they enabled the extraction of energy release rate that was independent of the height of the GB cohesive zone. For this, they relied on loading of the crack specimen followed by unloading. In the third approach, a crack specimen was subjected only to loading.

All the examined GB cracks showed brittle evolution, which in a few cases was also accompanied by facetted cleavage planes. Following the introduction of P impurities, the GB cracks mostly continued to be brittle, but occasionally void formation and crack-tip transformation were detected. A comparison of K_{IC}^{R} evaluations revealed that generally cracks propagated at a lower K_{IC}^{R} if the GB was inhabited by P impurities. But there were instances of increased or unaltered K_{IC}^{R} for increasing impurity coverage, implying locally improved or, at the least, unaffected GB cohesion, see Figure 13. Such localized strengthening behaviour was attributed to the extreme sensitivity of the K_{IC}^{R} to the original crack-tip location. Further, the localized crack-tip events such as crack-tip transformation, local deflection of cracks onto energetically less preferential planes and void formation, also significantly impacted the K_{IC}^{R}-values. As for the computed K_{IC}^{CZ}-values of the CZVEs of GBs, they were generally lower in P segregated GB cracks than in the pristine counterparts. However, for several CZVEs, similar K_{IC}^{CZ}-values for different impurity coverage were seen, see Figure 13(a). This shows that not only the absolute value of the impurity coverage matters but also the proximity of the impurities segregation sites relative to the cleavage plane influences the fracture toughness evaluation.

The K_{IC} based on the average energy release rate approach consistently reduced with increasing P impurity coverage, although to a varying degree for different

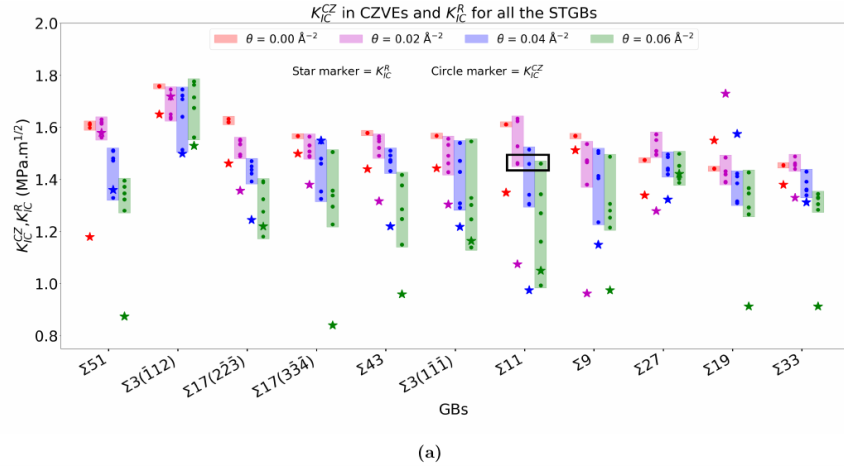

(a)

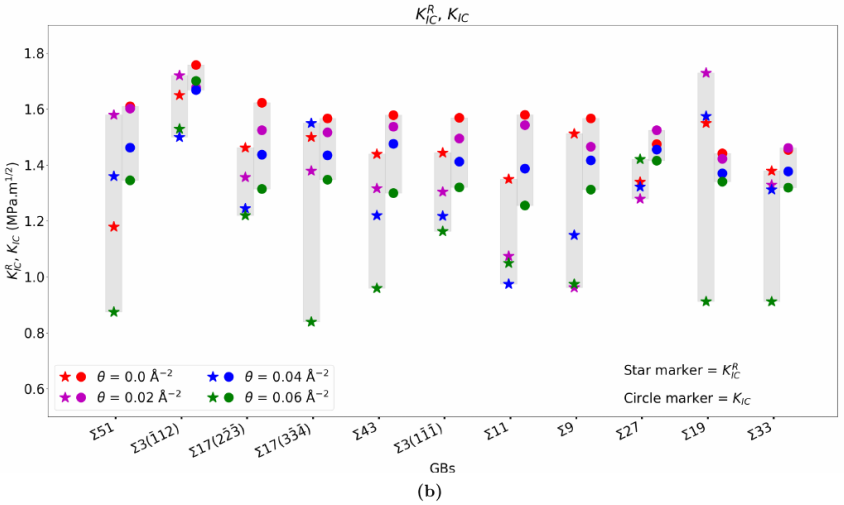

(b)

Figure 13: (a)K_{IC}^{CZ} and K_{IC}, and (b) K_{IC}^{R} and K_{IC} values for varying θ in the considered GBs. The encircled G_{I}^{CZ} values of the Σ11 GB in (a) represent the energy release rate for three CZVEs of interest with varying impurity coverage.

GBs, see Figure 13(b). This was true even for the GB cracks, which based on the evaluation of K_{IC}^{R}, supposedly were strengthened by P impurities. Thus, the average energy release rate based fracture toughness analysis was not affected by the localized crack-tip events and the pre-loading location of the crack-tip. Accordingly, in agreement with experimental observations [25, 29], it was concluded that P impurities reduce the fracture toughness of STGBs, which is an indication of the impurity enhanced GB embrittlement.

5.4 Paper IV - Extraction of scale-independent interfacial excess potential for twist grain boundaries

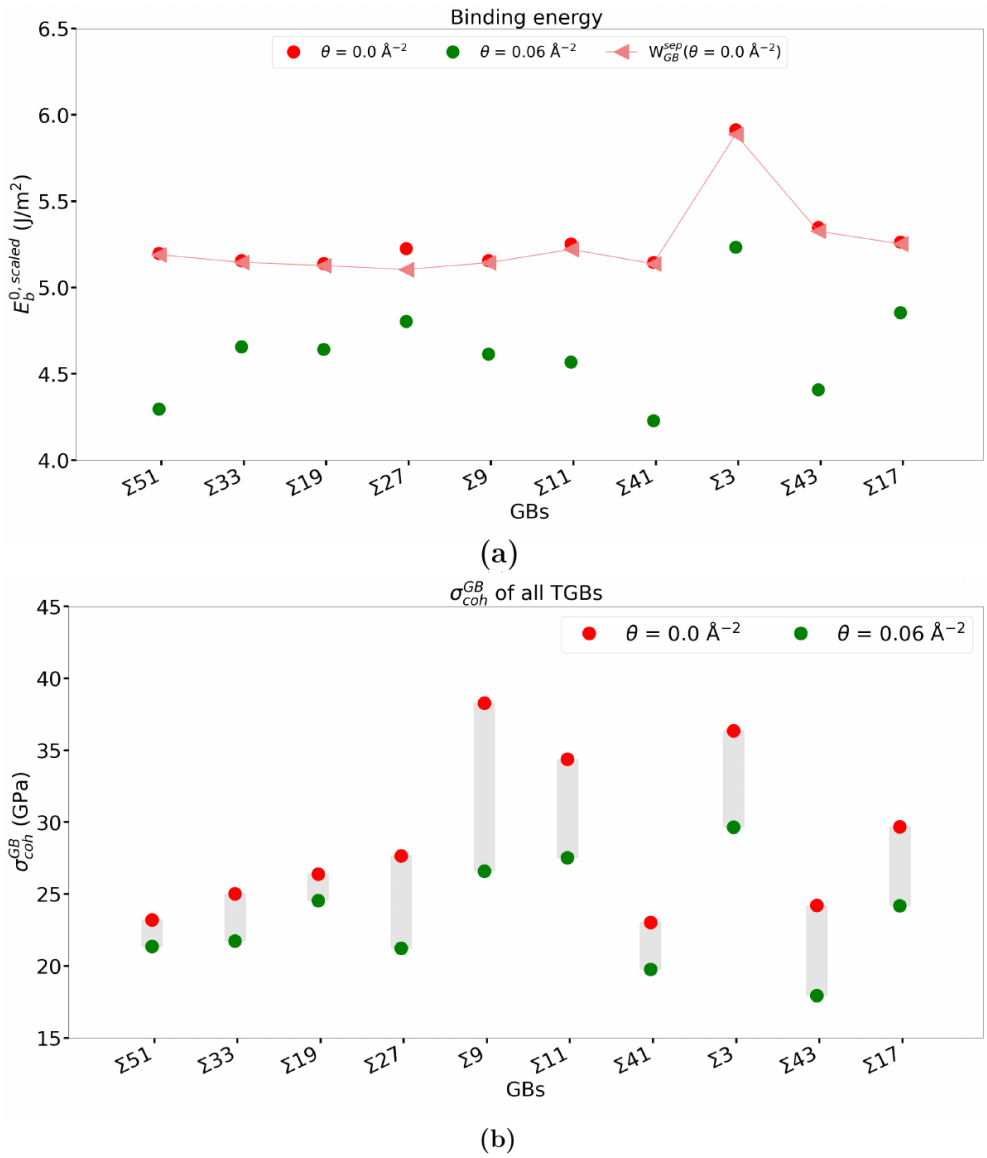

Figure 14: The impact of impurities on (a) $E_b^{0,scaled}$ and (b) σ_{coh}^{GB} for P impurity coverage $\theta = 0.0$ Å^{-2} and $= 0.06$ Å^{-2}.

A crack propagates via decohesion of two adjacent cleavage planes. To comprehend the energetics of decohesion between the two planes, the knowledge of

the interfacial excess potential that defines the traction-separation behaviour is essential. The extraction of the interfacial excess potential was infeasible employing the strategy adopted in Paper III. This motivated Paper IV, which focused on developing a strategy to extract scale-independent interfacial excess potential between the surfaces created by the propagation of a crack under K_I-controlled loading. The strategy was applied to several pristine $\langle 110 \rangle$ TGB cracks, and those with P impurity coverage of 0.06 Å^{-2} to investigate the impact of the impurities on the excess potential. Because the conventional universal binding energy relation (UBER) by Rose et al. [132] does not account for cleavage plane relaxations, as part of the approach, an elaborate fitting strategy of an extended UBER (xUBER) was proposed, to describe the decohesion energetics of the cleavage planes.

All the pristine TGB cracks showed brittle growth on the $\{110\}$ plane that had the lowest surface energy as per the potential used. Even when the GBs were covered with P impurities, all the cracks advanced on the same $\{110\}$ plane. However, pieces of debris of typically W-P clusters were formed on the cleavage plane. The developed strategy yielded the interfacial binding energy of the surfaces (analogous to the energy release rate), denoted by $E_b^{0,scaled}$, which concurred with the ideal work of separation (W_{GB}^{sep}), see Figure 14(a). The interfacial excess potential fit to the xUBER and the derived traction-separation data revealed that the P impurities reduce the energy release rate and peak stress (σ_{coh}^{GB}) for decohesion, see Figure 14(b). This highlights the embritteling effect of the impurities. The extracted excess potentials were scale-independent and invariant to the location of the CZVEs relative to the crack-tip. Furthermore, the proposed xUBER delineated the decohesion energetics as influenced by P impurities in the GB cracks.

6 Conclusions and outlook

6.1 Conclusions

In this thesis, atomistic modelling strategies have been developed to study and quantify the influence of P impurities on the fracture behaviour of cracks in W GBs. To this end, the material properties that play a vital role in deciding the mode of GB failure are investigated. Based on the ability of interatomic potentials to predict these fracture-relevant properties, a suitable interatomic potential is identified and an extensive atomistic fracture study is carried out.

In Paper I, although the considered potentials were built on the similar physical rationale, they were found to behave differently. Specifically, significant variations were noticed in their predictions for lattice and bond trapping of cracks. The lattice and bond trapping in turn impacted the fracture toughness, which triggered plastic deformation, despite the theoretical tendency of the cracks to undergo brittle growth was higher. Evident in this study is the sensitivity of the lattice and bond trapping to features like maximum interaction range and peak stress in the TS curves. Therefore, it becomes all the more important that the used potentials are fitted to an appropriate properties database and facilitate the estimation of these properties with a higher degree of accuracy. On the grounds of the aforementioned essentials, the MEAM-2 potential - the stand-out performer among all the considered potentials - is believed to be best suited for fracture investigations in pristine W.

Strain rate controlled tensile simulations (Paper II) and displacement controlled simulations of mode-I loaded GB cracks (Papers III and IV) were performed to study the impact of P impurities on the cohesion of GBs. From these investigations, it can be concluded that the P impurities weaken the GBs by screening the interaction across the GB interface. Consequently, the plastic mechanisms were suppressed all the while promoting brittle failure of the GBs. These observations of P induced GB embrittlement are in line with most experimental findings reported in the literature [25, 29].

Two modelling strategies were developed and implemented to quantify the influence of the impurities on the fracture toughness of GB cracks. The strategy designed in Paper III facilitated the evaluation of fracture toughness of individual CZVEs and its average value for the entire GB, from the measured energy release rate of CZVEs. The approach further enabled the assessment of variations in the local fracture toughness (in CZVEs) due to the impurity segregation sites and local mechanisms such as impurity induced crack deflections. As it was infeasible to extract a scale-independent interfacial excess potential from which the TS behaviour of GB cracks could be derived, a new procedure was developed in Paper IV. However, the decohesion energetics associated with the crack growth could not be described using the UBER formulations available in the literature. Prompted by this, xUBER, a modification to an existing UBER was proposed. The parameterized xUBER well represented the interfacial excess potential data, and the resulting binding energies of pristine GB cracks were consistent with the corresponding ideal work of separation values. The procedure was found to be applicable for impurity inhabited GBs as well, and could be used as input data for building constitutive laws for continuum scale fracture investigations.

In conclusion, the atomistic investigation herein supports the notion that P impurities bring about GB embrittlement and negatively affect the GB fracture toughness. Thus, the present work recovers and quantifies the experimentally observed effect of the impurities on GB fracture. Further, it provides a general modelling framework with novel atomistic approaches for investigating the impact of other types of impurities in W.

6.2 Suggested future work

One of the biggest challenges in atomistic modelling is to acquire interatomic potentials that possess sufficient transferability to ensure good predictability of all the relevant properties. To investigate the degradation of W components when subjected to the harsh conditions of a fusion reactor is a task that does not only involve GB embrittlement, but also other aspects such as neutron radiation damage, helium bubble formation and hydrogen isotope embrittlement [130]. Although the currently used potential has the ability to predict fracture properties well, it fails in other tasks such as describing the correct self-interstitial and vacancy formation energies. To overcome this hurdle, training and usage of machine learning potentials (MLPs) could be a viable route. Machine learning potentials generally have flexible formalisms, which enable a high-accuracy estimation of a wide range of material properties, as long as the fitting database is diverse [133]. Their predictability can be improved further by using active-learning algorithms, which allow on-the-fly refitting of the MLPs to new configurations that are originally absent in the fitting database [134]. Accordingly, because the fitting databases are commonly constructed from DFT, the MLPs produce results with close to DFT accuracy at a reduced numerical cost [133, 134]. This has led to an upsurge in the development of MLPs. Therefore, a possible avenue for future work is the development of versatile MLPs fitted to fracture related properties and apply them to large-scale atomistic fracture studies.

Investigation of the fracture behaviour of structural materials is indispensable for the assessment of nuclear reactor integrity. As it is a multiscale modelling endeavor, approaches to bridge the atomistic and higher time and length scale techniques should be explored [135, 136]. In this regard, especially the atomistic TS data in Paper IV, or the outlined data generation procedure, can be used as a starting point to generate GB interfacial constitutive relations for finite element method based modelling of GB cracks at the continuum level. This would provide a means to uncover higher time and length scale fracture phenomena.

References

[1] SJ Zinkle. Fusion materials science: Overview of challenges and recent progress. *Physics of Plasmas*, 12(5):058101, 2005.

[2] S Matsuda and K Tobita. Evolution of the ITER program and prospect for the next-step fusion DEMO reactors: status of the fusion energy R&D as ultimate source of energy. *Journal of Nuclear Science and Technology*, 50(4):321–345, 2013.

[3] J Linke, J Du, T Loewenhoff, G Pintsuk, B Spilker, I Steudel, and M Wirtz. Challenges for plasma-facing components in nuclear fusion. *Matter and Radiation at Extremes*, 4(5):056201, 2019.

[4] Y Ueda, K Schmid, M Balden, JW Coenen, T Loewenhoff, A Ito, A Hasegawa, C Hardie, M Porton, and M Gilbert. Baseline high heat flux and plasma facing materials for fusion. *Nuclear Fusion*, 57(9):092006, 2017.

[5] M Merola, F Escourbiac, R Raffray, P Chappuis, T Hirai, and A Martin. Overview and status of ITER internal components. *Fusion Engineering and Design*, 89(7-8):890–895, 2014.

[6] G Federici, A Zhitlukhin, N Arkhipov, R Giniyatulin, N Klimov, I Landman, V Podkovyrov, V Safronov, A Loarte, and M Merola. Effects of ELMs and disruptions on ITER divertor armour materials. *Journal of Nuclear Materials*, 337-339:684–690, 2005.

[7] J Pamela, A Bécoulet, D Borba, JL Boutard, L Horton, and D Maisonnier. Efficiency and availability driven R&D issues for DEMO. *Fusion Engineering and Design*, 84(2-6):194–204, 2009.

[8] M Rieth, JL Boutard, SL Dudarev, T Ahlgren, S Antusch, N Baluc, MF Barthe, CS Becquart, L Ciupinski, JB Correia, et al. Review on the EFDA programme on tungsten materials technology and science. *Journal of Nuclear Materials*, 417(1-3):463–467, 2011.

[9] M Rieth, SL Dudarev, SM Gonzalez De Vicente, J Aktaa, T Ahlgren, S Antusch, DEJ Armstrong, M Balden, N Baluc, MF Barthe, et al. A brief summary of the progress on the EFDA tungsten materials program. *Journal of Nuclear Materials*, 442(1-3):S173–S180, 2013.

[10] H Bolt, V Barabash, G Federici, J Linke, A Loarte, J Roth, and K Sato. Plasma facing and high heat flux materials–needs for ITER and beyond. *Journal of Nuclear Materials*, 307:43–52, 2002.

[11] P Norajitra, SI Abdel-Khalik, LM Giancarli, T Ihli, G Janeschitz, S Malang, IV Mazul, and P Sardain. Divertor conceptual designs for a fusion power plant. *Fusion Engineering and Design*, 83(7-9):893–902, 2008.

[12] D Maisonnier, D Campbell, I Cook, L Di Pace, L Giancarli, J Hayward, AL Puma, M Medrano, P Norajitra, M Roccella, et al. Power plant conceptual studies in Europe. *Nuclear Fusion*, 47(11):1524, 2007.

[13] A Giannattasio, Z Yao, E Tarleton, and SG Roberts. Brittle–ductile transitions in polycrystalline tungsten. *Philosophical Magazine*, 90(30):3947–3959, 2010.

[14] VA Makhlay, AN Bandura, OV Byrka, IE Garkusha, VV Chebotarev, VI Tereshin, and I Landman. Effect of preheating on the damage to tungsten targets after repetitive ITER elm-like heat loads. *Physica Scripta*, 2007(T128):239, 2007.

[15] T Hirai, E Bondarchuk, AI Borovkov, T Koppitz, J Linke, P Mertens, O Neubauer, A Panin, V Philipps, G Pintsuk, et al. Development and testing of a bulk tungsten tile for the JET divertor. *Physica Scripta*, 2007(T128):144, 2007.

[16] E Gaganidze, D Rupp, and J Aktaa. Fracture behaviour of polycrystalline tungsten. *Journal of Nuclear Materials*, 446(1-3):240–245, 2014.

[17] M Wirtz, I Uytdenhouwen, V Barabash, F Escourbiac, T Hirai, J Linke, T Loewenhoff, S Panayotis, and G Pintsuk. Material properties and their influence on the behaviour of tungsten as plasma facing material. *Nuclear Fusion*, 57(6):066018, 2017.

[18] L Gharaee. *First principles study of tungsten-based alloys: From defect thermodynamics to phase diagrams*. PhD thesis, Department of Chemistry and Chemical Engineering, Chalmers University of Technology, 2017.

[19] P Gumbsch, J Riedle, A Hartmaier, and HF Fischmeister. Controlling factors for the brittle-to-ductile transition in tungsten single crystals. *Science*, 282(5392):1293–1295, 1998.

[20] A Giannattasio and SG Roberts. Strain-rate dependence of the brittle-to-ductile transition temperature in tungsten. *Philosophical Magazine*, 87(17):2589–2598, 2007.

[21] V Philipps. Tungsten as material for plasma-facing components in fusion devices. *Journal of Nuclear Materials*, 415(1):S2–S9, 2011.

[22] Y Zhang, AV Ganeev, JT Wang, JQ Liu, and IV Alexandrov. Observations on the ductile-to-brittle transition in ultrafine-grained tungsten of commercial purity. *Materials Science and Engineering: A*, 503(1-2):37–40, 2009.

[23] BG Butler, JD Paramore, JP Ligda, C Ren, ZZ Fang, SC Middlemas, and KJ Hemker. Mechanisms of deformation and ductility in tungsten–a review. *International Journal of Refractory Metals and Hard Materials*, 75:248–261, 2018.

[24] V Nikolic, S Wurster, D Firneis, and R Pippan. Improved fracture behavior and microstructural characterization of thin tungsten foils. *Nuclear Materials and Energy*, 9:181–188, 2016.

[25] B Gludovatz, S Wurster, T Weingärtner, A Hoffmann, and R Pippan. Influence of impurities on the fracture behaviour of tungsten. *Philosophical Magazine*, 91(22):3006–3020, 2011.

[26] D Scheiber, R Pippan, P Puschnig, and L Romaner. Ab initio calculations of grain boundaries in bcc metals. *Modelling and Simulation in Materials Science and Engineering*, 24(3):035013, 2016.

[27] P Gumbsch. Brittle fracture and the brittle-to-ductile transition of tungsten. *Journal of Nuclear Materials*, 323(2-3):304–312, 2003.

[28] P Beardmore and D Hull. Deformation and fracture of tungsten single crystals. *Journal of the Less Common Metals*, 9(3):168–180, 1965.

[29] A Joshi and DF Stein. Intergranular brittleness studies in tungsten using Auger spectroscopy. *Metallurgical Transactions*, 1(9):2543–2546, 1970.

[30] G Bonny, A Bakaev, D Terentyev, and YA Mastrikov. Interatomic potential to study plastic deformation in tungsten-rhenium alloys. *Journal of Applied Physics*, 121(16):165107, 2017.

[31] A Hasegawa, M Fukuda, S Nogami, and K Yabuuchi. Neutron irradiation effects on tungsten materials. *Fusion Engineering and Design*, 89(7-8):1568–1572, 2014.

[32] M Rieth, SL Dudarev, SMG De Vicente, J Aktaa, T Ahlgren, S Antusch, DEJ Armstrong, M Balden, N Baluc, M-F Barthe, et al. Recent progress in research on tungsten materials for nuclear fusion applications in Europe. *Journal of Nuclear Materials*, 432(1-3):482–500, 2013.

[33] S Hofmann and H Hofmann. Influence of grain boundary segregation on mechanical properties of activated sintered tungsten. *Le Journal de Physique Colloques*, 46(C4):C4–633, 1985.

[34] KB Povarova, AS Drachinskii, and YUO Tolstobrov. Influence of microalloying on the cold brittleness temperature of tungsten. *Russ. Metall.*, (1):129–137, 1987.

[35] JR Stephens. *Effects of interstitial impurities on the low-temperature tensile properties of tungsten*, volume 2287. National Aeronautics and Space Administration, 1964.

[36] BC Muddle and DV Edmonds. Interfacial segregation and embrittlement in liquid phase sintered tungsten alloys. *Metal Science*, 17(4):209–218, 1983.

[37] JP Morniroli, M Gantois, M Lahaye, et al. Brittle fracture of polycrystalline tungsten. *Journal of Materials Science*, 20(1):199–206, 1985.

[38] M Grujicic, H Zhao, and GL Krasko. Atomistic simulation of $\Sigma 3(111)$ grain boundary fracture in tungsten containing various impurities. *International Journal of Refractory Metals and Hard Materials*, 15(5-6):341–355, 1997.

[39] GL Krasko. Effect of impurities on the electronic structure of grain boundaries and intergranular cohesion in tungsten. *International Journal of Refractory Metals and Hard Materials*, 12(5):251–260, 1993.

[40] Z Pan, LJ Kecskes, and Q Wei. The nature behind the preferentially embrittling effect of impurities on the ductility of tungsten. *Computational materials science*, 93:104–111, 2014.

[41] PAT Olsson and J Blomqvist. Intergranular fracture of tungsten containing phosphorus impurities: A first principles investigation. *Computational Materials Science*, 139:368–378, 2017.

[42] W Setyawan and RJ Kurtz. Effects of B, C, N, O, P and S impurities on tungsten $\sum 27$ [110]{552} and $\sum 3$ [110]{112} grain boundaries. Technical report, Pacific Northwest National Lab.(PNNL), Richland, WA (United States), 2013.

[43] S Plimpton. Fast parallel algorithms for short-range molecular dynamics. *Journal of Computational Physics*, 117(1):1–19, 1995.

[44] AP Thompson, HM Aktulga, R Berger, DS Bolintineanu, WM Brown, PS Crozier, PJ In't Veld, A Kohlmeyer, SG Moore, TD Nguyen, R Shan, MJ Stevens, J Tranchida, C Trott, and SJ Plimpton. LAMMPS - a flexible simulation tool for particle-based materials modeling at the atomic, meso, and continuum scales. *Computer Physics Communications*, 271:108171, 2022.

[45] TL Anderson. *Fracture mechanics: fundamentals and applications*. CRC press, 2005.

[46] AA Griffith. VI. The phenomena of rupture and flow in solids. *Philosophical Transactions of The Royal Society of London. Series A, containing papers of a mathematical or physical character*, 221(582-593):163–198, 1921.

[47] R Thomson, C Hsieh, and V Rana. Lattice trapping of fracture cracks. *Journal of Applied Physics*, 42(8):3154–3160, 1971.

[48] G Schoeck and W Pichl. Bond trapping of cracks. *Physica Status Solidi A*, 118(1):109–115, 1990.

[49] JR Rice. Dislocation nucleation from a crack tip: an analysis based on the Peierls concept. *Journal of the Mechanics and Physics of Solids*, 40(2):239–271, 1992.

[50] JR Rice. Mathematical analysis in the mechanics of fracture. In H. Liebowitz, editor, *Fracture: An Advanced Treatise*, volume 2 of *Mathematical Fundamentals*, chapter 3, pages 191–311. Academic Press, NY, 1968.

[51] F Nilsson. *Fracture Mechanics: From Theory to Applications*. Department of Solid Mechanics, Royal Institute of Technology, 1999.

[52] P Andric and WA Curtin. Atomistic modeling of fracture. *Modelling and Simulation in Materials Science and Engineering*, 27(1):013001, 2018.

[53] GC Sih, PC Paris, and GR Irwin. On cracks in rectilinearly anisotropic bodies. *International Journal of Fracture Mechanics*, 1(3):189–203, 1965.

[54] GC Sih and H Liebowitz. Mathematical theories of brittle fracture. In H. Liebowitz, editor, *Fracture: An Advanced Treatise*, volume 2 of *Mathematical Fundamentals*, chapter 2, pages 67–190. Academic Press, NY, 1968.

[55] KS Cheung and S Yip. A molecular-dynamics simulation of crack-tip extension: the brittle-to-ductile transition. *Modelling and Simulation in Materials Science and Engineering*, 2(4):865, 1994.

[56] A Neogi, M Alam, A Hartmaier, and R Janisch. Anisotropic failure behavior of ordered intermetallic tial alloys under pure mode-I loading. *Modelling and Simulation in Materials Science and Engineering*, 28(6):065016, 2020.

[57] AP Sutton and RW Balluffi. *Interfaces in crystalline materials*. Clarendon Press, 1995.

[58] M Lane. Interface fracture. *Annual Review of Materials Research*, 33(1):29–54, 2003.

[59] DS Lieberman and S Zirinsky. A simplified calculation for the elatic constants of arbitrarily oriented single crystals. *Acta Crystallographica*, 9(5):431–436, 1956.

[60] J Riedle, P Gumbsch, and HF Fischmeister. Cleavage anisotropy in tungsten single crystals. *Physical Review Letters*, 76(19):3594, 1996.

[61] JJ Möller and E Bitzek. Fracture toughness and bond trapping of grain boundary cracks. *Acta Materialia*, 73:1–11, 2014.

[62] JJ Möller. *Atomistic Simulations on Grain Boundary Fracture in Tungsten Bicrystals*, Diploma Thesis, Friedrich - Alexander - Universität Erlangen - Nürnberg. 2011.

[63] JJ Möller. *Atomistic Simulations of Crack Front Curvature Effects and Crack-Microstructure Interactions*. PhD thesis, Friedrich - Alexander - Universität Erlangen - Nürnberg, 2017.

[64] S Kohlhoff, P Gumbsch, and HF Fischmeister. Crack propagation in bcc crystals studied with a combined finite-element and atomistic model. *Philosophical Magazine A*, 64(4):851–878, 1991.

[65] WA Curtin. On lattice trapping of cracks. *Journal of Materials Research*, 5(7):1549–1560, 1990.

[66] P Gumbsch. *Atomistische Modellierung zweidimensionaler Defekte in Metallen: Risse, Phasengrenzflächen*. Dissertation, Universität Stuttgart, 1991.

[67] P Gumbsch and RM Cannon. Atomistic aspects of brittle fracture. *MRS Bulletin*, 25(5):15–20, 2000.

[68] P Gumbsch. Modelling brittle and semi-brittle fracture processes. *Materials Science and Engineering: A*, 319:1–7, 2001.

[69] M Marder. Effects of atoms on brittle fracture. *International Journal of Fracture*, 130(2):517–555, 2004.

[70] S Xu, JK Startt, TG Payne, CS Deo, and DL McDowell. Size-dependent plastic deformation of twinned nanopillars in body-centered cubic tungsten. *Journal of Applied Physics*, 121(17), 2017.

[71] EB Tadmor and N Bernstein. A first-principles measure for the twinnability of FCC metals. *Journal of the Mechanics and Physics of Solids*, 52(11):2507–2519, 2004.

[72] EB Tadmor and S Hai. A peierls criterion for the onset of deformation twinning at a crack tip. *Journal of the Mechanics and Physics of Solids*, 51(5):765–793, 2003.

[73] D Scheiber. *Theoretical Study of Grain Boundaries in Tungsten and Molybdenum*. PhD thesis, Karl-Franzens-Universität, Graz, (2016).

[74] P Lejček. Grain boundaries: description, structure and thermodynamics. *Grain boundary segregation in metals*, pages 5–24, 2010.

[75] V Randle. *The measurement of grain boundary geometry*. CRC Press, 2017.

[76] L Priester. *Grain boundaries: From Theory to Engineering*, volume 172. Springer Science & Business Media, 2012.

[77] D Wolf and JF Lutsko. On the geometrical relationship between tilt and twist grain boundaries. *Zeitschrift für Kristallographie-Crystalline Materials*, 189(1-4):239–262, 1989.

[78] D Wolf and S Yip. *Materials interfaces: atomic-level structure and properties*. Springer, 1992.

[79] D Terentyev, X He, A Serra, and J Kuriplach. Structure and strength of $\langle 110 \rangle$ tilt grain boundaries in bcc Fe: An atomistic study. *Computational materials science*, 49(2):419–429, 2010.

[80] W Setyawan and RJ Kurtz. Effects of transition metals on the grain boundary cohesion in tungsten. *Scripta Materialia*, 66(8):558–561, 2012.

[81] ML Kronberg and FH Wilson. Secondary recrystallization in copper. *Journal of The Minerals, Metals and Materials Society*, 1(8):501–514, 1949.

[82] NH Fletcher et al. Crystal interface models–a critical survey. *Advances in materials research*, 5:281–314, 1971.

[83] M Born and W Heisenberg. Zur quantentheorie der molekeln. *Annalen der Physik*, 379(9):1–31, 1924.

[84] RM Martin. *Electronic structure: basic theory and practical methods*. Cambridge university press, 2020.

[85] E Bitzek, P Koskinen, F Gähler, M Moseler, and P Gumbsch. Structural relaxation made simple. *Physical review letters*, 97(17):170201, 2006.

[86] AR Leach. *Molecular modelling: principles and applications*. Pearson education, 2001.

[87] D Frenkel and B Smit. *Understanding molecular simulation: from algorithms to applications*. Elsevier, 2023.

[88] EB Tadmor and RE Miller. *Modeling materials: continuum, atomistic and multiscale techniques*. Cambridge University Press, 2011.

[89] R Kjellander. *Statistical Mechanics of Liquids and Solutions: Intermolecular Forces, Structure and Surface Interactions*. CRC Press, 2019.

[90] AP Thompson, SJ Plimpton, and W Mattson. General formulation of pressure and stress tensor for arbitrary many-body interaction potentials under periodic boundary conditions. *The Journal of chemical physics*, 131(15):154107, 2009.

[91] DH Tsai. The virial theorem and stress calculation in molecular dynamics. *The Journal of Chemical Physics*, 70(3):1375–1382, 1979.

[92] HC Andersen. Molecular dynamics simulations at constant pressure and/or temperature. *The Journal of chemical physics*, 72(4):2384–2393, 1980.

[93] HJC Berendsen, JPM van Postma, WFV Van Gunsteren, ARHJ DiNola, and JR Haak. Molecular dynamics with coupling to an external bath. *The Journal of chemical physics*, 81(8):3684–3690, 1984.

[94] S Chandrasekhar. Stochastic problems in physics and astronomy. *Reviews of modern physics*, 15(1):1, 1943.

[95] R Biswas and DR Hamann. Simulated annealing of silicon atom clusters in langevin molecular dynamics. *Physical Review B*, 34(2):895, 1986.

[96] S Nosé. A unified formulation of the constant temperature molecular dynamics methods. *The Journal of chemical physics*, 81(1):511–519, 1984.

[97] S Nosé. A molecular dynamics method for simulations in the canonical ensemble. *Molecular physics*, 52(2):255–268, 1984.

[98] WG Hoover. Canonical dynamics: Equilibrium phase-space distributions. *Physical review A*, 31(3):1695, 1985.

[99] DJ Evans and BL Holian. The nose–hoover thermostat. *The Journal of chemical physics*, 83(8):4069–4074, 1985.

[100] N Metropolis, AW Rosenbluth, MN Rosenbluth, AH Teller, and E Teller. Equation of state calculations by fast computing machines. *The journal of chemical physics*, 21(6):1087–1092, 1953.

[101] MS Daw and MI Baskes. Semiempirical, quantum mechanical calculation of hydrogen embrittlement in metals. *Physical Review Letters*, 50(17):1285, 1983.

[102] MS Daw and MI Baskes. Embedded-atom method: Derivation and application to impurities, surfaces, and other defects in metals. *Physical Review B*, 29(12):6443, 1984.

[103] MS Daw, SM Foiles, and MI Baskes. The embedded-atom method: a review of theory and applications. *Materials Science Reports*, 9(7-8):251–310, 1993.

[104] MS Daw. Model of metallic cohesion: The embedded-atom method. *Physical Review B*, 39(11):7441, 1989.

[105] BJ Lee and MI Baskes. Second nearest-neighbor modified embedded-atom-method potential. *Physical Review B*, 62(13):8564, 2000.

[106] BJ Lee, MI Baskes, H Kim, and YK Cho. Second nearest-neighbor modified embedded atom method potentials for bcc transition metals. *Physical Review B*, 64(18):184102, 2001.

[107] Y Mishin. Interatomic potentials for metals. *Handbook of Materials Modeling: Methods*, pages 459–478, 2005.

[108] MI Baskes. Modified embedded-atom potentials for cubic materials and impurities. *Physical Review B*, 46(5):2727, 1992.

[109] MI Baskes, JS Nelson, and AF Wright. Semiempirical modified embedded-atom potentials for silicon and germanium. *Physical Review B*, 40(9):6085, 1989.

[110] MI Baskes, JE Angelo, and CL Bisson. Atomistic calculations of composite interfaces. *Modelling and Simulation in Materials Science and Engineering*, 2(3A):505–518, may 1994.

[111] E Bitzek, JR Kermode, and P Gumbsch. Atomistic aspects of fracture. *International Journal of Fracture*, 191:13–30, 2015.

[112] DS Dugdale. Yielding of steel sheets containing slits. *Journal of the Mechanics and Physics of Solids*, 8(2):100–104, 1960.

[113] GI Barenblatt. The mathematical theory of equilibrium cracks in brittle fracture. *Advances in applied mechanics*, 7:55–129, 1962.

[114] T Shimada, K Ouchi, Y Chihara, and T Kitamura. Breakdown of continuum fracture mechanics at the nanoscale. *Scientific reports*, 5(1):8596, 2015.

[115] JJ Möller, E Bitzek, R Janisch, H ul Hassan, and A Hartmaier. Fracture ab initio: A force-based scaling law for atomistically informed continuum models. *Journal of Materials Research*, 33(22):3750–3761, 2018.

[116] WS Ko and BJ Lee. Origin of unrealistic blunting during atomistic fracture simulations based on MEAM potentials. *Philosophical Magazine*, 94(16):1745–1753, 2014.

[117] G Bonny, D Terentyev, A Bakaev, P Grigorev, and D Van Neck. Many-body central force potentials for tungsten. *Modelling and Simulation in Materials Science and Engineering*, 22(5):053001, jun 2014.

[118] LX Liu, XC Li, YC Chen, WY Hu, GN Luo, F Gao, and HQ Deng. Evaluation of tungsten interatomic potentials for radiation damage simulations. *Tungsten*, 2:3–14, 2020.

[119] MW Finnis and JE Sinclair. A simple empirical N-body potential for transition metals. *Philosophical Magazine A*, 50(1):45–55, 1984.

[120] GJ Ackland and R Thetford. An improved N-body semi-empirical model for body-centred cubic transition metals. *Philosophical Magazine A*, 56(1):15–30, 1987.

[121] S Han, LA Zepeda-Ruiz, GJ Ackland, R Car, and DJ Srolovitz. Interatomic potential for vanadium suitable for radiation damage simulations. *Journal of Applied Physics*, 93(6):3328–3335, 2003.

[122] J Wang, YL Zhou, M Li, and Q Hou. A modified W–W interatomic potential based on ab initio calculations. *Modelling and Simulation in Materials Science and Engineering*, 22(1):015004, 2013.

[123] MC Marinica, L Ventelon, MR Gilbert, L Proville, SL Dudarev, J Marian, G Bencteux, and F Willaime. Interatomic potentials for modelling radiation defects and dislocations in tungsten. *Journal of Physics: Condensed Matter*, 25(39):395502, 2013.

[124] PAT Olsson. Semi-empirical atomistic study of point defect properties in BCC transition metals. *Computational Materials Science*, 47(1):135–145, 2009.

[125] XW Zhou, RA Johnson, and HNG Wadley. Misfit-energy-increasing dislocations in vapor-deposited CoFe/NiFe multilayers. *Physical Review B*, 69(14):144113, 2004.

[126] J Riedle, P Gumbsch, HF Fischmeister, VG Glebovsky, and VN Semenov. Fracture studies of tungsten single crystals. *Materials Letters*, 20(5-6):311–317, 1994.

[127] C Bohnert, NJ Schmitt, SM Weygand, O Kraft, and R Schwaiger. Fracture toughness characterization of single-crystalline tungsten using notched micro-cantilever specimens. *International Journal of Plasticity*, 81:1–17, 2016.

[128] J Ast, M Göken, and K Durst. Size-dependent fracture toughness of tungsten. *Acta Materialia*, 138:198–211, 2017.

[129] J Ast, JJ Schwiedrzik, J Wehrs, D Frey, MN Polyakov, J Michler, and X Maeder. The brittle-ductile transition of tungsten single crystals at the micro-scale. *Materials & Design*, 152:168–180, 2018.

[130] RG Abernethy, JSK L Gibson, A Giannattasio, JD Murphy, O Wouters, S Bradnam, LW Packer, MR Gilbert, M Klimenkov, M Rieth, et al. Effects of neutron irradiation on the brittle to ductile transition in single crystal tungsten. *Journal of Nuclear Materials*, 527:151799, 2019.

[131] S Kalácska, J Ast, PD Ispánovity, J Michler, and X Maeder. 3D HR-EBSD characterization of the plastic zone around crack tips in tungsten single crystals at the micron scale. *Acta Materialia*, 200:211–222, 2020.

[132] JH Rose, JR Smith, and J Ferrante. Universal features of bonding in metals. *Physical Review B*, 28(4):1835, 1983.

[133] H Mori and T Ozaki. Neural network atomic potential to investigate the dislocation dynamics in bcc iron. *Physical Review Materials*, 4(4):040601, 2020.

[134] L Zhang, G Csányi, E Van Der Giessen, and F Maresca. Atomistic fracture in bcc iron revealed by active learning of gaussian approximation potential. *npj Computational Materials*, 9(1):217, 2023.

[135] V Yamakov, E Saether, and EH Glaessgen. Multiscale modeling of intergranular fracture in aluminum: constitutive relation for interface debonding. *Journal of materials science*, 43:7488–7494, 2008.

[136] T Xu, R Stewart, J Fan, X Zeng, and A Yao. Bridging crack propagation at the atomistic and mesoscopic scale for bcc-fe with hybrid multiscale methods. *Engineering Fracture Mechanics*, 155:166–182, 2016.

Scientific publications

Author contribution statement

Paper I: Effects of interatomic potential on fracture behaviour in single- and bicrystalline tungsten (Published).
The idea of the paper was conceived in discussion with my co-authors. I participated in the later stage of the fitting of the potential. I performed the MS modelling and the analysis of the results. I wrote the original draft. The co-authors assisted in reviewing and editing the manuscript.

Paper II: Atomistic investigation of the impact of phosphorus impurities on the tungsten grain boundary decohesion (Published).
The idea of the paper was conceived in discussion with my co-authors. I performed the hybrid MC/MD and tensile modelling, and the analysis of the results. I wrote the parts of the original draft on hybrid MC/MD and tensile modelling, and the corresponding results. Co-author Olsson wrote the other parts of the original draft and all authors assisted in reviewing and editing the manuscript.

Paper III: Phosphorus driven embrittlement and atomistic crack behaviour in tungsten grain boundaries (Published).
The idea of the paper was conceived in discussion with my co-authors. I performed the MS modelling and the formal analysis of the results. I wrote the original draft. The co-authors assisted in reviewing and editing the manuscript.

Paper IV: Atomistic assessment of interfacial interaction potential in tungsten twist grain boundaries (Submitted for publication).
The idea of the paper was conceived in discussion with my co-authors. I performed the MS modelling and the formal analysis of the results. I wrote the original draft. The co-authors assisted in reviewing and editing the manuscript.

Printed by Media-Tryck, Lund 2024 NORDIC SWAN ECOLABEL 3041 0903

Division of Mechanics, Materials & Component Design,
Department of Mechanical Engineering Sciences
Faculty of Engineering
Lund University
ISBN 978-91-8104-078-4